Journal of Ionic Liquids 3 (2023) 100060

Contents lists available at ScienceDirect

Journal of Ionic Liquids

journal homepage: www.elsevier.com/locate/jil

Dynamics, cation conformation and rotamers in guanidinium ionic liquids with ether groups

Daniel Rauber[a,*], Frederik Philippi[b], Bernd Morgenstern[a], Josef Zapp[c], Björn Kuttich[d], Tobias Kraus[a,d], Tom Welton[b], Rolf Hempelmann[a], Christopher W.M. Kay[a,e]

[a] Department of Chemistry, Saarland University, Campus B2.2, Saarbrücken, Federal Republic of Germany
[b] Department of Chemistry, Molecular Sciences Research Hub, Imperial College London, White City Campus, London W12 0BZ, UK
[c] Pharmaceutical Biology, Saarland University, Campus B 2.3, Saarbrücken 66123, Federal Republic of Germany
[d] INM-Leibniz Institute for New Materials, Campus D2.2, Saarbrücken, Federal Republic of Germany
[e] London Centre for Nanotechnology, University College London, 17-19 Gordon Street, London W1E 6BT, UK

ARTICLE INFO

Keywords:
Ionic liquid
Structure-property relation
Dynamics
Conformation
Nuclear magnetic
Resonance

ABSTRACT

Ionic liquids are modern materials with a broad range of applications, including electrochemical devices, the exploitation of sustainable resources and chemical processing. Expanding the chemical space to include novel ion classes allows for the elucidation of novel structure-property relationships and fine tuning for specific applications. We prepared a set of ionic liquids based on the sparsely investigated pentamethyl guanidinium cation with a 2-ethoxy-ethyl side chain in combination with a series of frequently used anions. The resulting properties are compared to a cation with a pentyl side chain lacking ether functionalization. We measured the thermal transitions and transport properties to estimate the performance and trends of this cation class. The samples with imide-type anions form liquids at ambient temperature, and show good transport properties, comparable to imidazolium or ammonium ionic liquids. Despite the dynamics being significantly accelerated, ether functionalization of the cation favors the formation of crystalline solids. Single crystal structure analysis, *ab initio* calculations and variable temperature nuclear magnetic resonance measurements (VT-NMR) revealed that cation conformations for the ether- and alkyl-chain-substituted are different in both the solid and liquid states. While ether containing cations adopt compact, curled structures, those with pentyl side chains are linear. The Eyring plot revealed that the curled conformation is accompanied by a higher activation energy for rotation around the carbon-nitrogen bonds, due to the coordination of the ether chain as observed by VT-NMR.

Introduction

Ionic liquids have become an important class of soft materials with widespread applicability in diverse applications. Their combination of properties typically associated with both conventional molecular liquids and high-temperature molten salts is of interest for uses in academia and industry. Typical properties of ionic liquids include negligible volatility, ionic conductivity and high thermal, chemical and electrochemical stability (Philippi and Welton, 2021). In addition, they are able to dissolve a wide range of organic, inorganic and biological substances, including salts of alkaline metals, dyes and macromolecules such as cellulose, lignin, chitin or proteins. Consequently, the uses of ionic liquids range from electrolytes in electrochemical devices (Watanabe et al., 2017), such as rechargeable batteries, supercapacitors and fuel cells, over functional materials (Zhang et al., 2016), to the utilization of renewable resources (Mahmood et al., 2017). Many potential uses are in the field of sustainable development (Quintana et al., 2022), which makes the investigation of these modern liquid materials highly pertinent.

To further optimize the performance of ionic liquids in a given technical implementation, the properties of the incorporated fluid must be suited ideally to the required purpose (Philippi and Welton, 2021). In general, the macroscopic properties of ionic liquids, such as viscosity, conductivity or useable thermal range, are considered when practical applications have to be developed or optimized. However, the macroscopic behavior of these complex fluids is governed by their chemical structure and resulting microscopic interactions (Hayes et al., 2015). The situation for ionic liquids in particular is difficult as multiple interactions and interwoven effects have to be considered. These include strong, long-rang Coulombic forces, hydrogen-bonds, dipole and dispersion interactions, solvophobic effects as well as influences from ion conformation and ion flexibility or the formation of aggregates (Wang et al., 2020). Due to the intricate interplay between composition, interactions

* Corresponding author.
E-mail address: daniel.rauber@uni-saarland.de (D. Rauber).

https://doi.org/10.1016/j.jil.2023.100060
Received 17 March 2023; Received in revised form 17 June 2023; Accepted 29 June 2023

and dynamics, the search for sophisticated structure-property relationships is greatly needed in the field of ionic liquids (Philippi and Welton, 2021; Hayes et al., 2015; Lundin et al., 2021). This is especially true as the number of possible ionic liquids is much larger than that of molecular solvents by orders of magnitude (Hayes et al., 2015).

Compared to molecular fluids, ionic liquids suffer from limitations in respect of higher melting points and viscosities (Rauber et al., 2021a). The higher melting points of ionic liquids reduces the range in which they can be applied on the low temperature side. This is crucial for instance in many electrochemical devices or processes, where operating temperatures below ambient are needed. The higher viscosities of ionic liquids are linked to the slower dynamics on molecular scale as a result of the strong, long-rang Coulombic interactions. High viscosities are undesirable in most applications and impede the exchange and distribution of substances and/or heat. This sets limits for the transport of substances, for instance of electroactive species or the reagents in chemical reactions, and generally slows down processes. Finding strategies to optimize ionic liquids for low melting points and low viscosities is much needed as most applications with ionic liquids can benefit from the implementation of these concepts.

Functional group manipulation is a tool for modifying the chemical structures of ionic liquids, resulting in changes of their ion conformations, arrangements and interactions, ultimately altering the macroscopic behavior (Philippi and Welton, 2021). Chemical functionalities are mainly incorporated into the organic cations of ionic liquids. In most cases incorporating functional groups into their alkyl chains leads to an increase in the melting point and viscosity (Yu et al., 2012). This is the result of a loss in conformational flexibility as result of the functionalization arising from higher barriers of rotation and intensified interactions with the anions due to electronic effects leading to increased charge localization. In spite of the generally undesired influence of functional groups on the solidification temperatures and dynamics, the reverse trend is found when ether groups are incorporated into the cations of ionic liquids. This boost of ionic liquid properties by ether groups is a general effect found for many different cations, *e.g.* phosphonium, (Hofmann et al., 2022; Philippi et al., 2017, 2020a; Kashyap et al., 2013; Tsunashima and Sugiya, 2007) ammonium, (Rauber et al., 2021a; Philippi et al., 2020a; Rauber et al., 2021b; Yoshii et al., 2020), piperidinium (Nokami et al., 2018) and imidazolium (Lall-Ramnarine et al., 2017; Shimizu et al., 2013).

In addition to studying the influence of functional group in known cations, investigating novel cations promises to expanding the chemical space and possible property-combinations of ionic liquids. Literature studies are often restricted to a set of established, commercially available cation-anion combinations. Therefore, the cation subclasses of ammonium, phosphonium, imidazolium and pyridinium are almost exclusively studied (Singh and Savoy, 2020). In this contribution we present the synthesis and properties of novel aprotic ionic liquids based on the pentamethyl guanidinium (PMG) cation paired with various anions commonly used for ionic liquids. The 2-ethyl-ethoxy chain, where the oxygen atom is in γ-position, was chosen as the side group. The molecular structures of the cations and anions investigated in this study are shown in Scheme 1. The properties of the 2-ethoxyethyl-pentamethyl guanidinium cation, $[2O2PMG]^+$, paired with the bis(trifluoromethanesulfonyl)imide anion, $[NTf_2]^-$, were compared to the isostructural pentyl-pentamethyl guanidinium cation $[C_5PMG]^+$, where the oxygen atom is replaced by a methylene unit. Comparing the properties of the ionic liquids with the two different cations in combination with the widely used benchmark imide-type anion allows for direct investigations of the ether group influence on the resulting macroscopic properties. As these ionic liquids had low melting points and we were not able to crystallize them, we also included the sample consisting of pentyl-pentamethyl guanidinium and hexafluorophosphate $[PF_6]^-$ anion that formed crystals suitable for single crystal structural analysis.

Guanidinium ionic liquids have delocalized π-electrons, similar to imidazolium and pyridinium cations which are both aromatic nitrogen heterocycles. While the delocalized system in the guanidium cations is in a Y-shape (*cf.* Y-aromaticity Dworkin et al. 2005, Gobbi and Frenking 1993), the latter two have a cyclic π-system. Therefore, in guanidinium cations, rotations around the C–N bonds in the delocalized system are possible, contrary to the rigid ring-shaped systems. Hexaalkyl guanidinium ionic liquids were recently shown to have good thermal and transport properties (Rauber et al., 2018). Such ionic liquids are thought to be suitable as lubricants (Huang et al., 2017), gas absorbents (Królikowski et al., 2022), plastic crystals (Biernacka et al., 2022), or electrolytes (Fang et al., 2009, 2011). Some representatives of the guanidinium ionic liquids were also found to be environmentally benign (Pratap Singh et al., 2017) or show only low toxicity (Yu et al., 2016; Carrera et al., 2010). In addition, protic guanidinium ionic liquids, stemming from the superbase guanidine show interesting characteristics in ease of synthesis, stability and behavior of the acidic proton towards formation of hydrogen bonds or proton transfer.

Materials and methods

Details about the synthesis and NMR resonances of the investigated ionic liquids and precursors are given in the supporting information. The identity and purity of the samples was checked by multinuclear NMR spectroscopy. Absence of halides in the final ionic liquids was tested with aqueous silver nitrate solution. Prior to all physicochemical measurements the samples were dried in high vacuum for at least two days. Handling of the dried samples was carried out using Schlenk techniques or a Labmaster 130 glove box (MBraun, Germany). Densities ρ were determined using a calibrated commercial pycnometer (Neubert Glas, Germany) and a PROLINE RP 1845 thermostat (LAUDA, Germany) for temperature control from 25 °C to 95 °C in steps of 10 °C.

Thermal properties

Crystallization (T_c), glass (T_g), cold crystallization (T_{cc}), solid-solid transitions (T_{ss}) and melting (T_m) temperatures were determined by means of differential scanning calorimetry (DSC). Samples of approximately 10 mg were hermetically sealed in the glove box and measured on a DSC 1 STARe instrument (Mettler Toledo) using cooling by liquid nitrogen. The samples were heated to 120 °C with a scanning rate of +5 °C min^{-1} to remove thermal history. The samples were then subjected to cooling with –1 °C min^{-1} to –120 °C followed by a dynamic heating of +1 °C min^{-1} to 120 °C. The slow scanning rates were used to avoid the formation of glasses instead of crystallization as the result of quenching (Gómez et al., 2015).

Decomposition temperatures (T_d) were determined using thermogravimetric analysis (TGA) on a TGA/DSC 1 STARe device. For this purpose, the samples were heated with +10 °C min^{-1} from 30 °C to 700 °C under a constant stream of nitrogen. The decomposition temperatures obtained from the TGA traces are given as extrapolated onset temperatures.

Transport properties

The dynamic viscosity was measured on a Physica 301 MCR301 rheometer (Anton Paar, Austria), which was placed on a vibration isolating table. The measuring setup used cone-plate geometry with a CP50-1 cone of 49.95 mm diameter in a nitrogen flushed oven. The tip of the cone had a distance of 0.101 mm to the plate. Viscosities at shear rates between 50 and 150 s^{-1} (30 linearly spaced values, 10 s measurement times) were measured at each temperature. Temperature stability before and during each measurement was recorded and checked to be below ±0.01 °C. As there was no shear-rate dependent behavior observed (Newtonian flow) the viscosity values for each temperature were averaged. The process was repeated from 25 °C to 105° in steps of 5 °C to construct the temperature-dependent viscosity curves. Uncertainty

of the viscosity values is ±1.5% estimated from measurement of commercial viscosity standards, repeated measurements and comparison to established ionic liquid samples.

The specific conductivity of the samples was measured by impedance spectroscopy using a SP-150 potentiostat (Biologic, France) in combination with a commercial conductivity cell (WTW, Germany). The conductivity cell consisted of two rectangular platinized platinum electrodes and had a nominal cell constant of 0.5 cm^{-1}. The cell was freshly platinized and the cell constant determined with repeated measurements of commercial standards. The sealed conductivity probe with the samples under argon was immersed in a PROLINE RP 1845 thermostat (LAUDA, Germany) to control the temperature during the impedance measurements. For each temperature three impedance spectra with 5, 10 and 15 mV applied voltage were recorded in the frequency range of 200 kHz to 1 Hz using 50 logarithmic steps. The resistance of the electrolytes obtained this way were averaged for each temperature and had a maximum deviation of ±1%. The specific conductivity κ was then calculated as the cell constant divided by the electrolyte resistance. The process was repeated from 25 °C to 100 °C in 5 °C steps to construct the temperature-dependent curves of the specific conductivity. Temperature stability of the thermostat bath was within the range of ±0.01 °C. Uncertainty of the specific conductivity measurements is ±2%, which was estimated from commercial conductivity standards and repeated measurements. The molar conductivity Λ_M was calculated from the specific conductivity κ, density ρ and molar mass M of the ionic liquids according to Eq. (1).

$$\Lambda_M = \frac{\kappa}{c} = \frac{\kappa \cdot M}{\rho} \tag{1}$$

Self-diffusion coefficients were measured by NMR spectroscopy using the pulsed field gradient stimulated spin echo (PFGSTE) pulse sequence with bipolar gradients and longitudinal eddy current delay (ledbpgp2s in the Bruker pulse program library). Measurements were conducted on an Avance Neo 500 Spectrometer (Bruker, Germany) with a TCI Prodigy cryo-probe and a BCU II temperature unit. All dried samples were placed in the inserts of coaxial tubes (1 mm diameter) under argon and were flame-sealed to avoid uptake of ambient moisture. The narrow tube geometry allowed for faster temperature equilibration and minimized convection. The diffusion measurements were performed after shimming, careful calibration of the pulses, determination of the longitudinal relaxation time T_1 and a pair of values for the diffusion time Δ and the duration of the pulsed field gradient δ yielding sufficient signal attenuation (≈ 5% signal intensity for the resonances in the spectrum with highest applied gradient strength). For the measurements Δ and δ were kept constant with the strength of the pulsed field gradient g being varied from 2% to 95% of the probe's maximum gradient strength (65.7 G cm^{-1}) in linear spacing. Gradient shape was that of a smoothed rectangle. In total 16 experiments for each of the 16 spectra with different strength of the pulsed field gradient were recorded. Relaxation delay between the individual experiments was seven times the determined T_1 minus the acquisition time. The ^1H nucleus was used for the determination of the cation self-diffusion coefficients D_{s+}, while anion self-diffusion coefficients D_{s-} where measured utilizing the ^{19}F nucleus. The self-diffusion coefficients D_{si} were obtained from fitting of the Stejskal–Tanner Eq. (2):

$$I = I_0 \cdot \exp\left(-D_{si}\delta^2 g^2 \gamma^2 \left(\Delta - \frac{\delta}{3}\right)\right) \tag{2}$$

with γ being the gyromagnetic ratio of the investigated nucleus. The given procedure was applied in the range of 5 °C to 90 °C in steps of 5 °C to construct the temperature-dependent curves of the self-diffusion coefficients. Uncertainty of the self-diffusion coefficients is ±2%, estimated from repeated measurements and comparison to literature values for molecular and ionic liquids.

Temperature-dependent transport properties Y (Y being viscosity η, specific conductivity κ, molar conductivity Λ_M or self-diffusion coefficients D_{si}) were fitted using the Vogel–Fulcher–Tammann (VFT) Eq. (3):

$$Y = Y_0 \cdot \exp\left(\frac{B_Y}{T - T_{0,Y}}\right) \tag{3}$$

with Y_0, B_Y and $T_{0,Y}$ being empirical fitting parameters. In the case of viscosity, the values for B_Y are positive (viscosity decrease with T), while for the other transport quantities B_Y takes negative values (increasing with T). From the VFT fitting parameters Angell's strength factor δ_Y for a particular transport quantity can be calculated as B_Y divided by $T_{0,Y}$. The magnitude of Angell's strength factor is a measure for the fragility of a liquid, where fragility increases for smaller values of δ_Y (Alba-Simionesco and Tarjus, 2022). It should be noted that δ_Y is often termed D in literature, which is not used here to avoid confusion with the self-diffusion coefficients, also usually termed D.

The activation energy $E_{a,Y}$ for the transport properties was determined by the Arrhenius Eq. (4) as the slope of the Arrhenius plot ($\ln(Y)$ *vs.* T^{-1}) at the stated temperature multiplied with the negative of the gas constant R.

$$Y = Y_0 \cdot \exp\left(-\frac{E_{a,Y}}{RT}\right) \tag{4}$$

Single crystal structure analysis

Crystals suitable for single crystal X-ray crystallography were prepared from ethanol-water mixtures by slow evaporation of the organic solvent. The data set was collected using a Bruker X8 Apex diffractometer. Graphite-monochromated molybdenum K_α-line radiation (λ = 0.71073Å) was used. Data were collected at 142 ± 2 K ([2O2PMG][PF_6]) and 152 ± 2 K ([C_5PMG][PF_6]) and corrected for absorption effects using the multi-scan method. The structure was solved by direct methods using SHELXS-97 (Sheldrick, 2008) and was refined by full matrix least squares calculations on F^2 (SHELXL2018, Sheldrick 2015) in the graphical user interface Shelxle (Hübschle et al., 2011). Additional refinement details are given in the supporting information. Crystal structures are available from the Cambridge Crystallographic Data center under deposition number 2238194 ([2O2PMG][PF_6]) and 2238197 ([C_5PMG][PF_6]).

Computations

Ab initio calculations were performed using the Gaussian software package, Revision E.01 (Frisch et al., 2013). The potential energy surfaces (PES) and minimum energy geometries were obtained and validated at the MP2/cc-pVTZ//B3LYP-GD3BJ/6-311+G(d,p) level of theory following the setup described in our preceding work.

Small angle X-Ray scattering

Samples for small angle X-ray scattering (SAXS) were placed in thin walled borosilicate capillaries and immediately flame-sealed. The samples were measured in a Xeuss 2.0 (Xenocs, France) scattering setup with a Genix 3D as X-ray source generating radiation at the copper -line (wavelength λ = 1.54 Å). Scattered photons were recorded using the detectors Pilatus3 R 1M and a Pilatus 100 K. The scattered intensity was recorded in the range of the scattering vector q from 0.02 $Å^{-1}$ to 3.01 $Å^{-1}$, with $q = |\vec{q}| = 4\pi \sin(\theta)\lambda^{-1}$ and the scattering angle 2θ. The obtained two-dimensional isotropic scattering patterns were radially averaged to obtain the one-dimensional scattering curves. The peak positions discussed in the main part were fitted using Lorentzian functions.

Nuclear magnetic resonance spectroscopy

Variable temperature NMR spectra were recorded on an Avance Neo 500 Spectrometer (Bruker, Germany) with a TCI Prodigy cryo-probe and a BCU II temperature unit. The dried bulk ionic liquids were

Table 1
Thermal transition temperatures (Crystallization temperature T_c, glass transition temperature T_g, cold crystallization temperature T_{cc} and melting temperature T_m) from DSC measurements with scan rates of ±1 °C min^{-1}, decomposition temperatures T_d under N_2 flow and heating rates of ±10 °C min^{-1}, and density ρ at 25 °C (measured in supercooled state for some samples).

Ionic liquid	T_c /°C	T_g /°C	T_{cc} /°C	T_m /°C	T_d /°C	$\rho^{25°C}$ / g mL^{-1}
[2O2PMG][FSI]	−32	–	–	−6	305	1.2674
[2O2PMG][NTf_2]	−20	–	–	26	405	1.3472
[2O2PMG][BETI]	−12	–	–	29	403	1.4204
[2O2PMG][OTf]	30	–	–	56	331	–
[2O2PMG][BF_4]	64	–	–	86	398	–
[2O2PMG][PF_6]	52	–	–	87	411	–
[2O2PMG][TFA]	−8	–	–	36	214	1.1674
[C_5PMG][NTf_2]	–	−79	−28	−1	425	1.3109
[C_5PMG][PF_6][a)]	62	–	–	65	433	–

[a)]Additional solid-solid transitions at 50 °C upon cooling and at 21 °C, 52 °C and 61 °C upon heating.

flame-sealed in the inner tube of coaxial tubes. Deuterated 1,1,2,2-tetrachloroethane (99.5% D) (Deutero, Germany) was placed in the outer tube and used for locking, shimming and as reference. Measurements were conducted from 0 °C to 90 °C in steps of 2.5 °C in case of [2O2PMG][NTf_2] and from –15 °C to 90 °C for [C_5PMG][NTf_2].

Results and discussion

Thermal properties and density

The temperature range in which ionic liquids can be applied is restricted by the stability of their liquid state. Therefore, the solidification (lower limit) and thermal decomposition (upper limit) behavior is of great practical interest when it comes to the characterization of novel ionic liquids. The thermal transitions as observed by differential scanning calorimetry (DSC) are given in Table 1.

All of the investigated ionic liquids, except [C_5PMG][NTf_2], crystallize upon cooling (T_c) and then melt again upon heating (T_m), similar to most organic ionic compounds. Only the pentyl containing ionic liquid with the bis(trifluoromethanesulfonyl)imide anion, [C_5PMG][NTf_2], forms a glass upon cooling (T_g), followed by liquefaction of the glass with subsequent cold crystallization (T_{cc}) upon heating and melting of the crystal. The hexasubstituted guanidinium ionic liquids with the ether side chain therefore seem to be good crystal formers.

Although most samples form crystals instead of glasses, the samples show pronounced supercooling as seen from the differences between T_c and T_m. The lowest difference is found for the [PF_6]$^-$ ionic liquid with the ether group, being only 22 °C while the largest difference was 46 °C for [2O2PMG][NTf_2]. For other guanidinium samples with protic, pentasubstituted cations or hexaalkylated guanidiniums with two butyl chains, the absence of crystallization and occurrence of only glassy solids has been found (Rauber et al., 2018). The similar cation 2-methoxy-ethyl-pentamethyl guanidinium with [NTf_2]$^-$ has been reported to show no melting point down to temperatures as low as –60 °C (Fang et al., 2009). The absence of crystallization in the latter literature report might be due the experimental conditions, where fast scan rates of –10 °C min^{-1} were applied.

Although the only room temperature ionic liquids (T_m < 25 °C) in this set are the ether bis(fluorosulfonyl)imide, [2O2PMG][FSI], and the pentyl-substituted [NTf_2]$^-$ sample, several of the other ionic liquids could be obtained in liquid state at 25 °C for prolonged times before crystallization. These in particular were the ether-substituted ionic liquids with the anions [NTf_2]$^-$, bis(pentafluoroethylsulfonyl)imide [BETI]$^-$ and trifluoroacetate [TFA]$^-$, which have melting points slightly above 25 °C. Therefore, the density and transport quantities of these ionic liquids could be obtained starting from 25 °C, whereas the density and transport properties of the samples with the triflate [OTf]$^-$, tetrafluoroborate [BF_4]$^-$ and hexafluorophosphate anion [PF_6]$^-$ were not measured any further. The occurrence of pronounced supercooling is a frequent observation for ionic liquids and result from the intended destabilization of the crystalline state (Gómez et al., 2015).

Substitution of the ether oxygen with a methylene group decreases the melting point by 27 °C for the sample with the [NTf_2]$^-$ anion and by 22 °C for the one with the [PF_6]$^-$ anion. This trend is contrary to what is observed for the melting or glass transition point of other ionic liquid classes, for instance imidazolium (Lall-Ramnarine et al., 2017), ammonium (Rauber et al., 2021a, 2021b) or phosphonium (Hofmann et al., 2022; Philippi et al., 2017, 2020a) and might be attributed to the altered cation conformation (see the results from the crystal structure analysis, the *ab initio* calculations and variable temperature NMR measurements below) allowing for more stable crystal lattices. This is also in accordance with the finding that for all these pentamethyl guanidinium ionic liquids with ether substituents melting points rather than glass transitions have been found. Contrary to the situation in these guanidinium ionic liquids, mainly glass transitions or lowered melting points are reported for many other ionic liquids upon ether functionalization. For these other cation classes the lower liquefaction temperatures are the result of unfavorable ordered crystalline states due to the altered cation conformation (Philippi et al., 2020a, 2018).

The trends in the melting points of the ether-substituted ionic liquids with the same cation can be rationalized by the influence of entropic effects with differences between the anions. The ether ionic liquids with the lowest melting points have highly flexible anions of the imide-type that change their conformation between *cis* and *trans* form when regarding the C–S···S–C dihedral angle (Johansson et al., 1998; Canongia Lopes et al., 2008; Suarez et al., 2015; Palumbo et al., 2015). Thus the three imide anions have a higher degree of conformational entropy in the liquid state compared to the crystal, where the anion conformations are fixed and not able to interconvert. In contrast to the flexible imides, the anions of higher symmetry, [BF_4]$^-$ and [PF_6]$^-$, have only one conformer and therefore no contribution to the increase in conformational entropy upon melting. Consequently, the samples with these anions show the highest melting points of the investigated ionic liquids.

Decomposition temperatures T_d, as obtained by TGA are reported in Table 1, (TGA curves are given in the supporting information) and correlate to the proton affinity and nucleophilicity of the anions' corresponding acids (Rauber et al., 2023). Therefore, the highest T_d values are found for the ionic liquids with the [NTf_2]$^-$, [BETI]$^-$, [BF_4]$^-$ and [PF_6]$^-$ anions stemming from the acids with the lowest proton affinities. Ether functionalization slightly decreases the decomposition temperatures by approximately 25 °C. Similar anion-dependent trends have also been reported for other ionic liquid with other cation classes (Xue et al., 2018). Decomposition temperature for the guanidinium ionic liquid are similar to other cation classes and overall quite high. For instance for

Table 2
Viscosity η and activation energy of the viscous flow $E_{a,\eta}$ at 25 °C, fitting parameters η_0, B_η and $T_{0,\eta}$ following the VFT fitting (Eq. (3)), as well as Angell's strength factor for the viscosity δ_η. All coefficients of determination $R^2 \geq 0.99999$ for the VFT fitting data.

Ionic liquid	$\eta^{25°C}$ / mPa s	η_0 / 10^{-1} mPa s	B_η / K	$T_{0,\eta}$ / K	δ_η	$E_{a,\eta}^{25°C}$ / kJ mol^{-1}
[2O2PMG][FSI]	76.3	2.011 ± 0.038	854.2 ± 6.2	154.3 ± 0.6	5.54 ± 0.05	30.5 ± 0.3
[2O2PMG][NTf$_2$]	65.5	2.237 ± 0.046	730.3 ± 6.2	169.6 ± 0.6	4.31 ± 0.04	32.6 ± 0.5
[2O2PMG][BETI]	129	1.625 ± 0.028	803.7 ± 4.7	177.8 ± 0.4	4.52 ± 0.03	40.8 ± 0.6
[2O2PMG][TFA]	157	0.920 ± 0.023	871.7 ± 6.7	181.0 ± 0.5	4.82 ± 0.04	47.0 ± 0.6
[C$_5$PMG][NTF$_2$]	99.6	1.665 ± 0.021	819.9 ± 3.7	169.9 ± 0.3	4.83 ± 0.02	38.4 ± 0.6

the frequently used 1-butyl-3-methyl imidazolium cation decomposition temperatures of 419 °C for the [NTf$_2$]$^-$ anion, 399 °C when paired with [BF$_4$]$^-$ and 421 °C in combination with [PF$_6$]$^-$ have been reported (Cao and Mu, 2014).

The densities of the ionic liquid that could be obtained in the liquid state at 25 °C are given in Table 1. For the ionic liquids with the ether-containing cations the densities increase in the order [TFA]$^-$ < [FSI]$^-$ < [NTf$_2$]$^-$ < [BETI]$^-$ thus following the trend to be expected from the molecular weight and the number of the heavier heteroatoms. Comparing the density of [2O2PMG][NTf$_2$] with the pentyl analogue reveals a significantly higher density of the former. This comparatively large difference cannot be rationalized by the increase in molecular weight when exchanging the CH$_2$ group with an oxygen atom. As it was previously shown for other ionic liquids with ether groups, the difference in the densities can be explained by an altered conformation of the cation upon introduction of the ether functionality; whereby the ether chain with oxygen functionality in γ-position adopts a curled conformation with a dihedral angle X–C–C–O (similar to ϕ_2 as shown in Scheme 1), X being the atom to which the side chain is attached (X = N or P), of approximately 60°. For the hydrocarbon chain the side chain adopts a linear conformation with an X–C–C–C dihedral angle of approximately 180°. This change in the cation conformation leads to a more compact arrangement for the ionic liquids with ether chains, which manifests in the higher experimental densities, also seen in the densities calculated for the crystals of the two cations with the [PF$_6$]$^-$ anions, see supporting information. The temperature-dependent densities showed a linear progression in the investigated range. The experimental values and corresponding linear fitting parameters are given in the supporting information.

Transport properties

Viscosity

Viscosity plays a central role for ionic liquids as it limits many practical applications. It is generally desirable to obtain ionic liquids with low viscosities, since this aids improvement of their performance in many applications. Consequently, the viscosity is a central subject of investigation when evaluating the potential of new ionic liquid structures. The viscosity and activation energy values of the ionic liquids that could be obtained as liquids at 25 °C as well as the VFT-fitting data and Angell's strength factor for the T-dependent viscosity are given in Table 2. The course of the viscosity with temperature is plotted in Fig. 1, the experimental values are given in the supporting information.

For the ionic liquids with the [2O2PMG]$^+$ cation the viscosity at 25 °C increases in the order [NTf$_2$] < [FSI] < [BETI] < [TFA], thus the samples with imide-type ions are the most fluid. This trend reflects the order found for the melting points of the ether ionic liquids, although that the position of the [FSI]$^-$ and [NTf$_2$]$^-$ are interchanged. The higher fluidity of the [NTf$_2$]$^-$ anion despite its higher molecular mass might have its reason in the different underlying mechanism for the translational relaxation (Borodin et al., 2010). This assumption is also supported by the higher Angell fragility parameters found for [2O2PMG][FSI]. Temperatures in which [NTf$_2$]$^-$ ionic liquids have lower viscosities than the [FSI]$^-$ ones with a common cation are also

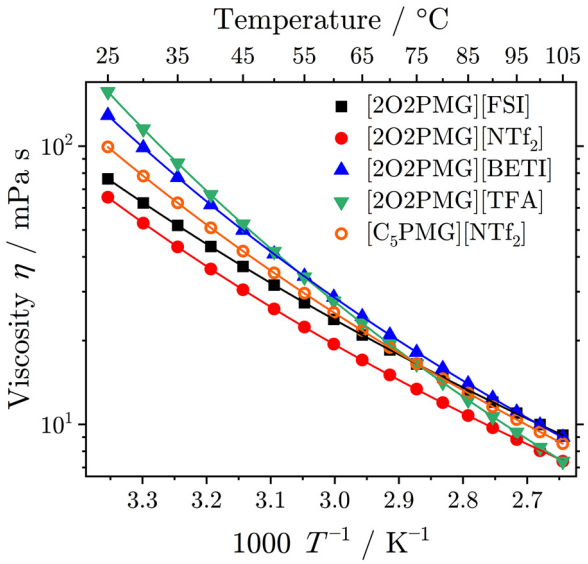

Fig. 1. Temperature-dependent viscosity of the investigated pentamethyl guanidinium ionic liquids. Drawn lines are the VFT-fits according to Eq. (3).

reported for instance for tetraalkyl ammonium-based representatives (Rauber et al., 2021a).

Similar to other ionic liquids the incorporation of ether chains with oxygen in γ-position leads to a decrease in viscosity. Exchanging the ether oxygen atom in the side group of the guanidinium ionic liquids with a methylene group results in a pronounced increase in viscosity by the factor of 1.5 For protic guanidinium ionic liquids the viscosity ratio of alkyl- to ether-substituted ones at 25 °C is 1.6 (Rauber et al., 2023), while for other cation classes, both higher and lower numbers are found. For instance for imidazolium-systems with single ether functionalization and the [NTf$_2$]$^-$ anion, increases in viscosity from 1.1 to 1.3 upon removal of the ether functionality were found (Lall-Ramnarine et al., 2017), while for ammonium- and phosphonium-based ionic liquids with the same anion the values of viscosity increase up to a factor of 2.0 (Hofmann et al., 2022; Philippi et al., 2017; Rauber et al., 2021b).

The temperature-dependent viscosity reveals a different T-dependence of the viscous flow for the investigated ionic liquids. The activation energies of viscous flow at 25 °C reveal the same order as the absolute values of the viscosity, although the positions of the [FSI]$^-$ and [NTf$_2$]$^-$ sample have interchanged. Due to the different T-dependence of the activation energies, presumably from different structural relaxation mechanisms as a result of altered anion sizes and flexibility, the order of the viscosities might also be interchanged at different temperatures (Philippi et al., 2022a). While showing the highest values at ambient temperature, the lowest viscosity is found for the [TFA]$^-$ anion at 105 °C. At this temperature the viscosity values increase in the order [TFA] ≈ [NTf$_2$] < [BETI] ≈ [FSI]. This altering is also indicated by the different activation energy changes upon increasing T. Temperature-dependent activation energies for

Table 3
Molar conductivity Λ_M and activation energy for the molar conductivity E_{a,Λ_M} at 25 °C, fitting parameters $\Lambda_{M,0}$, B_{Λ_M} and T_{0,Λ_M} following the VFT fitting according to Eq. (3) including Angell strength factor for the molar conductivity δ_{Λ_M}. All coefficients of determination $R^2 \geq 0.99999$ for the VFT fitting.

Ionic liquid	$\Lambda_M^{25°C}$ / S cm^2 mol^{-1}	$\Lambda_{M,0}$ / S cm^2 mol^{-1}	B_{Λ_M} / K	T_{0,Λ_M} / K	δ_{Λ_M}	$E_{a,\Lambda_M}^{25°C}$ / kJ mol^{-1}
[2O2PMG][FSI]	0.777	257.7 ± 5.2	−869.8 ± 7.8	148.2 ± 0.9	5.87 ± 0.06	28.5 ± 0.3
[2O2PMG][NTf$_2$]	0.767	246.8 ± 5.8	−832.5 ± 9.0	153.9 ± 1.0	5.41 ± 0.07	29.1 ± 0.2
[2O2PMG][BETI]	0.357	228.6 ± 5.7	−805.0 ± 8.6	173.7 ± 0.9	4.63 ± 0.05	36.8 ± 0.5
[2O2PMG][TFA]	0.283	209.9 ± 6.0	−673.3 ± 8.6	196.2 ± 1.0	3.43 ± 0.05	45.5 ± 0.7
[C$_5$PMG][NTf$_2$]	0.539	267.8 ± 5.2	−828.1 ± 7.0	164.8 ± 0.7	5.02 ± 0.05	33.5 ± 0.2

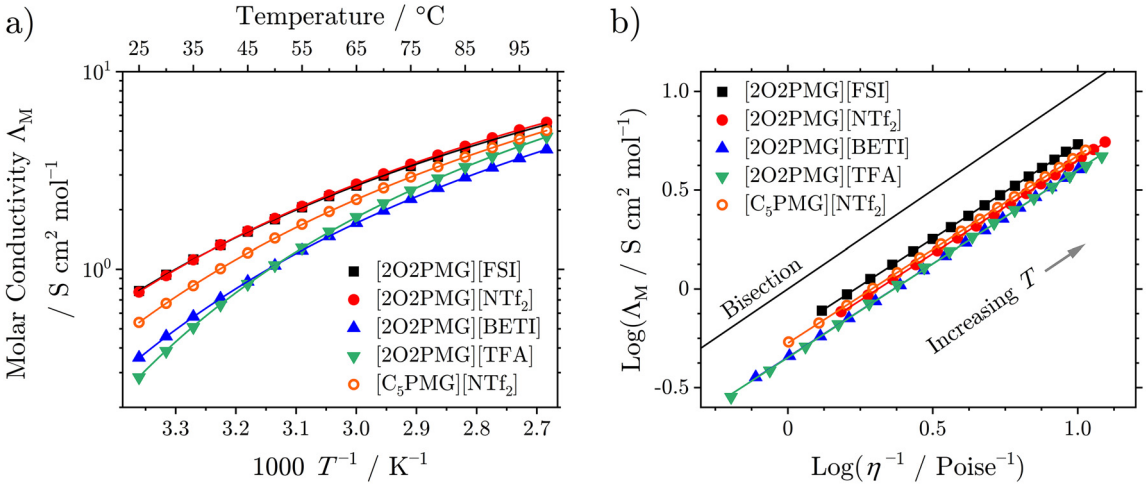

Fig. 2. (a) Temperature-dependent molar conductivity of the investigated guanidinium ionic liquids. Drawn lines are the VFT-fits (Eq. (3)). (b) Walden plot of the samples with bisection (often termed 'ideal KCl line') with drawn lines as linear fits.

transport properties are a common finding for ionic liquids. Therefore, the T-dependent data are usually fitted by the phenomenological VFT Eq. (3) instead of an Arrhenius-type fitting (Eq. (4)), also in agreement with the findings here (Wang et al., 2020; Harris and Kanakubo, 2016). The temperature-dependence of the activation energy in the context of the VFT model is the Angell strength factor δ_Y, which has low values for fluids with high 'fragility' (temperature-dependent $E_{a,Y}$), while so-called 'strong' liquids have a constant activation energy (Harris and Kanakubo, 2016). Similar to other ionic liquids, the guanidinium samples in this set have quite small values for δ_η, thus are highly fragile liquids. For comparison, the ionic liquid consisting of the commonly used 1-butyl-3-methyl imidazolium cation $[C_4C_1im]^+$ adopts a value of 4.50 for the Angell strength factor of viscosity when paired with the $[FSI]^-$ anion (Nazet et al., 2015), 4.65 in combination with $[NTf_2]^-$ (Harris et al., 2007), and 5.98 when the $[BETI]^-$ anion is utilized (Nazet et al., 2015).

Molar conductivity and Walden plot

Conductivity is a central, important quantity of electrolytes when used in electrochemical applications. Consequently, the investigation of the conductivity of novel ionic liquids is of great importance when these are considered for use in electrochemistry and electrochemical devices. The values for the molar conductivity Λ_M at 25 °C, the activation energy at this temperature as well as the T-dependent fitting parameters following the VFT Eq. (3) are given in Table 3. The corresponding plot of the T-dependent molar conductivity is shown in Fig. 2a. Experimental values and fitting parameters of the guanidinium ionic liquids' specific conductivity are given in the supporting information.

For the ionic liquids with the $[2O2PMG]^+$ cation the order of the molar conductivity at 25 °C is the same as found for the melting points. One would expect that the conductivities would also follow the same trend as the viscosities, but it can be seen that the $[FSI]^-$ and $[NTf_2]^-$ samples have swapped their position. However, the difference between these two imide-type samples is small and there is a crossover in the molar conductivity at approximately 40 °C. Replacing the pentyl side group in the cation by a 2-ethoxy-ethyl group increases the molar conductivity at 25 °C by a factor of 1.42, which is quite close to the factor for the viscosity decrease. The activation energies of the molar conductivity at 25 °C show the same order as for the viscosity with the values for the viscosity being larger by a factor of 1.03 ([2O2PMG][TFA]) to 1.15 ([C$_5$PMG][NTf$_2$]).

Similar to the viscosity data, the molar conductivities showed a clear deviation from the Arrhenius-type behavior (Fig. 2a), but could be well fitted with the VFT Eq. (3). Furthermore, the sample [2O2PMG][TFA] shows a more pronounced T-dependence, which manifests in the stronger increase in molar conductivity for the same temperature interval compared to the other ionic liquids in this set.

The reciprocal correlation of viscosity and molar conductivity is to be expected, as these two transport quantities are connected by the Walden relation (Eq. (5)).

$$\Lambda_M \propto \left(\eta^{-1}\right)^t \tag{5}$$

with t being a factional exponent close to unity. Plotting the logarithm of the reciprocal viscosity (fluidity) *vs.* the logarithm of the molar conductivity yields straight lines with the slope of t. This so-called Walden plot is shown in Fig. 2b. The detailed fitting results are given in the

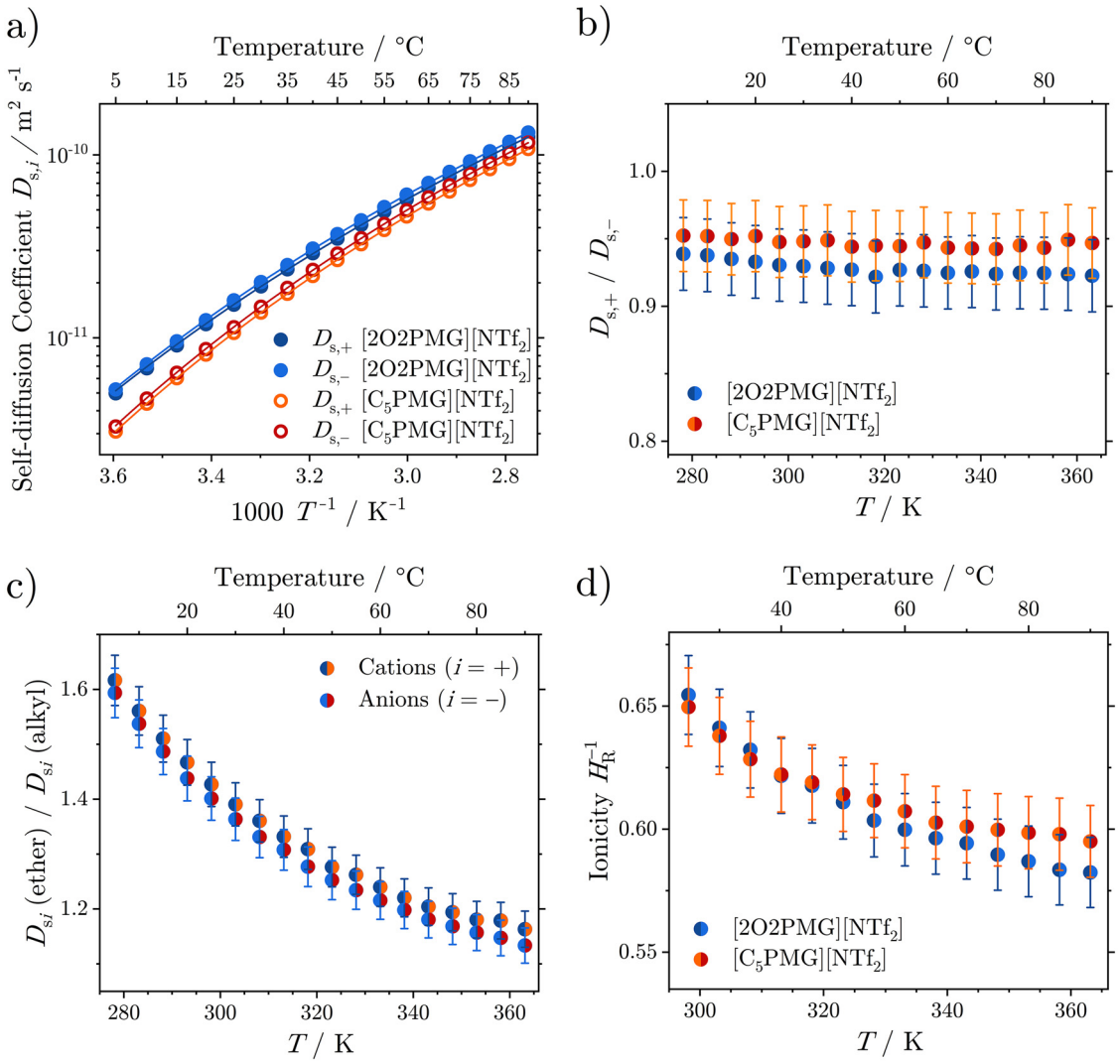

Fig. 3. (a) Temperature-dependent self-diffusion coefficients of the $[NTf_2]^-$ pentamethyl guanidinium ionic liquids. Drawn lines are the VFT fits according to Eq. (3). The ratios of the self-diffusion coefficient for (b) cation and anion of the same ionic liquids and (c) of ether to alkyl sample. (d) T-dependence of the reciprocal Haven ratios H_R^{-1}.

supporting information. All of the obtained slopes t are in the narrow interval from 0.945 to 0.952. Literature values for other ionic liquids are also observed to be in a similar range of values. For instance for the prototypical 1-alkyl-3-methyl-imidazolium ionic liquids $[C_xC_1im]^+$ the Walden exponents t have been found to rise from 0.89 to 0.95 when the alkyl-chain is elongated from ethyl (x = 2) to octyl (x = 8) (Harris and Kanakubo, 2015). For protic guanidinium ionic liquids t values from 0.92 to 0.97 have been reported (Rauber et al., 2018). All samples show comparatively low distances from the bisection in the Walden plot, the so called 'ideal KCl line', in agreement with literature findings for aprotic ionic liquids with these anions. The vertical (or horizontal) distance to the bisection has been occasionally used to quantify the degree of association in the ionic liquids by comparison to an ideally diluted electrolyte. It is generally assumed that this ideal electrolyte behavior, forming the bisection of the Walden plot, is satisfied by a 0.01 molar aqueous solution of potassium chloride. However, recent works have shown that this is not the case, so some care should be taken in interpreting the results of the Walden plot as deviation from ideal electrolyte behavior (Schreiner et al., 2010; Harris, 2019). Nevertheless, the 'ideal KCl line' as a collectively used reference line still gives valuable information about the behavior in comparison to other ionic liquids (or electrolytes). The quite small distance to the bisection of the Walden plot shows that the guanidinium ionic liquid of this sample set are 'good' ionic liquids according to the Walden classification (Harris, 2019), thus can be assumed to show a low amount of neutral species or ion aggregation. Higher distances from the bisection ('poor' ionic liquids) are for instance found for aprotic ionic liquids with long hydrocarbon chains (Yuan et al., 2018) or protic ionic liquids with lower differences in the pK_a values of the acid and base forming the ionic liquid, where a higher amount of neutral precursors is expected to be found (Angell et al., 2012). The distance to the bisection of the Walden plot can be quantified by the 'ionicity' value obtained by the Walden method I_W. The obtained values for the pentamethyl guanidinium ionic liquids at 25 °C are included in Table 4. The values at other temperatures are given in the supporting information. With increasing temperature, a slight decrease in the Walden ionicity is observed. This is similar to the results found for the reciprocal Haven ratio, which is regarded an alternative measure for 'ionicity', as discussed in the next section.

Self-diffusion coefficients and relations to other transport properties

Self-diffusion coefficients of the individual ions give microscopic information about the dynamics of ionic liquids. The separation of the self-diffusion coefficient for cations and anions (and other possible species dissolved in the ionic liquid) using different signals in high resolution

Table 4
Self-diffusion coefficients D_{si}, their ratio, the ionicities determined as reciprocal Haven ratio H_R^{-1} and by the Walden plot method I_W. All values are given for 25 °C.

Ionic liquid	D_{s+} / 10^{-11} m^2 s^{-1}	D_{s-} / 10^{-11} m^2 s^{-1}	D_{s+} / D_{s-}	H_R^{-1}	I_W
[2O2PMG][FSI]	1.33 ± 0.03	1.76 ± 0.04	0.76 ± 0.02	0.671 ± 0.016	0.593 ± 0.015
[2O2PMG][NTf$_2$]	1.52 ± 0.03	1.60 ± 0.03	0.95 ± 0.03	0.655 ± 0.016	0.502 ± 0.013
[2O2PMG][BETI]	0.773 ± 0.016	0.734 ± 0.015	1.05 ± 0.03	0.631 ± 0.015	0.461 ± 0.012
[2O2PMG][TFA]	0.554 ± 0.011	0.656 ± 0.013	0.84 ± 0.02	0.624 ± 0.015	0.445 ± 0.011
[C$_5$PMG][NTf$_2$]	1.06 ± 0.02	1.14 ± 0.03	0.93 ± 0.03	0.650 ± 0.016	0.535 ± 0.013

NMR allows more detailed insights about the contribution of the individual ions. The self-diffusion coefficients of the ionic liquids that could be obtained as liquids at 25 °C are summarized in Table 4.

For the self-diffusion coefficients at 25 °C a similar ranking as for the other transport properties is found, so the sample with the largest D_{si} values show the lowest viscosities and highest conductivities. The self-diffusion coefficients of [2O2PMG][FSI] reveal slower diffusion of the cation, but faster diffusion of the anion compared to the [NTf$_2$]$^-$ with the same cation. Overall the [2O2PMG][NTf$_2$] shows a slightly faster average diffusion than the [FSI]$^-$ counterpart in spite of its larger anion. For all samples, besides [2O2PMG][BETI], the anion diffuses faster than the cation. This is not surprising as the [BETI]$^-$ anion is also the heaviest and largest anion in the sample (see the reciprocal connection by the Stokes–Einstein Eq. (8)). However, when calculating the ion radius by *ab initio* methods, assuming spherical ion geometry, the radii of both cations are slightly higher than that of the [BETI]$^-$ anion. The ratio of the cation and anion self-diffusion coefficients are furthermore in good agreement with the reciprocal ratio of cation and anion radii (see supporting information). The only sample, where there the ratio of the self-diffusion coefficients is higher than expected from the ion radii, is [2O2PMG][TFA]. This might be attributed to the greater basicity of the triflate anion compared to those of the imide-type anions, allowing for stronger cation-anion interactions. Increased ion interaction affects the individual ion translational movements leading to smaller differences between the self-diffusion coefficients of cation and anion. The molecular weight ratio of the ions seems to play only a minor role on the ratio of the self-diffusion coefficients in an ionic liquid, as both [NTf$_2$]$^-$ and [BETI]$^-$ have significantly higher molar masses than the used guanidinium cations.

Comparing the self-diffusion coefficients of the ether substituted to the alkyl substituted cation reveals that the oxygen atom in γ-position of the side chain accelerates the self-diffusion of the cation by a factor of 1.43 and of 1.40 for the anion. Therefore, the ether functionalization accelerates the translational dynamics of both ions in a similar way, which indicates that the introduction of the heteroatom reduces the long-ranging Coulombic interactions leading to faster dynamics (Philippi et al., 2022b).

The Nernst–Einstein Eq. (6) can be used to calculate the molar conductivity, if the self-diffusion coefficients of all ions are known.

$$\Lambda_{M,NE} = \frac{F^2}{RT}\sum_{i=1}^{n} z_i^2 D_{s,i} \tag{6}$$

with F the Faraday constant and z_i the charge of the ion i. The Nernst–Einstein Eq. (6) was derived for ions in infinitely diluted solutions and is frequently used to quantify the deviation of real electrolytes from the ideal electrolyte. For real electrolytes, such as the bulk ionic liquids, the molar conductivity calculated from the Nernst–Einstein equation can be compared to the experimental values Λ_M, obtained by impedance spectroscopy. In the case of aprotic ionic liquids, the experimental molar conductivities are always lower than the ones calculated from the Nernst–Einstein equation. This ratio is the reciprocal of the Haven ratio H_R, Eq. (7), and sometimes referred to as 'ionicity' (Ueno et al., 2010).

$$H_R^{-1} = \frac{\Lambda_M}{\Lambda_{M,NE}} \tag{7}$$

The values of H_R^{-1} ('ionicity') are often interpreted as the extent of ion pairing or ion aggregation in the ionic liquids (Nordness and Brennecke, 2020; McEldrew et al., 2021). As these neutral species or clusters with reduced overall charge would not contribute to the conductivity or at least to a lesser extent than expected assuming isolated ions, a lower conductivity is found in experiments. Although lacking an underlying theory, the H_R^{-1} values are helpful to understand trends in ionic liquids which helps optimization of conductivity for practical implementations. This still holds true, even when other rationalizations for the deviation of the ionic liquid conductivities from ideal electrolyte behavior are considered. Alternative explanations for the H_R^{-1} cover for example charge-transfer from anion to cation leading to overall reduced charges z_i (Hollóczki et al., 2014; Philippi et al., 2022c), the occurrence of different states of diffusion analogous to semi-conductors (Feng et al., 2019) or velocity cross-correlations due to momentum conservation (Harris, 2010; Kashyap et al., 2011; Mariani et al., 2021). For the ether-containing pentamethyl guanidinium ionic liquids the H_R^{-1} values at 25 °C are in a comparatively narrow range in the order [FSI]$^-$ > [NTf$_2$]$^-$ > [BETI]$^-$ > [TFA]$^-$. The reciprocal Haven ratio of the [NTf$_2$]$^-$ ionic liquids with the 2-ethoxy-ethyl chain and the pentyl chain is nearly identical, which is contrary to other cation classes, where the ether substitution usually lead to a decrease in H_R^{-1} (Rauber et al., 2021a; Hofmann et al., 2022; Rauber et al., 2021b). Prototypical ionic liquids with the 1-butyl-3-methyl imidazolium cation have similar H_R^{-1} numbers, *e.g.* 0.62 in combination with the [NTf$_2$]$^-$ anion (Tokuda et al., 2005) or 0.52 for [TFA]$^-$ (Tokuda et al., 2004). For other guanidinium ionic liquids, both protic and aprotic ones with imide anions, a similar range for the values of the reciprocal Haven ratio, from 0.50 to 0.74 at 25 °C has been reported (Rauber et al., 2018).

Temperature-dependent self-diffusion coefficients of the [NTf$_2$]$^-$ samples were measured to gain more insight into the effect of the ether chain on the movements on the molecular scale. The VFT fits (Eq. (3)) are given in Table 5 and the results plotted in Fig. 3a.

The ratios between the self-diffusion coefficients for the samples show hardly any T-dependence, see Fig. 3b indicating that the change in activation energy is quite similar for the translational movement of cation and anion. The fact that the ratio of the self-diffusion constants of cation and anion in a specific ionic liquid remain constant was anticipated by the fact that the activation energies at 25 °C are identical within experimental error and that the Angell strength parameters for the self-diffusion coefficients are also similar.

Contrary to the ratio of the ion self-diffusion of a particular ionic liquid, the ratio of the self-diffusion coefficients between the ions of the ether substituted and the pentyl substituted ionic liquid show a significant change with increasing temperature, compare Fig. 3c. While the ether to alkyl ratio of the self-diffusion coefficients is approximately 1.60 at 5 °C, it decreases to roughly 1.15 at 90 °C. The finding that the ratio of transport properties for ether to alkyl ionic liquids diminishes with increasing temperature has also been shown for other cation classes, with the difference between ether and alkylated samples being higher when multiple ether substituents are used (Rauber et al., 2021a; Philippi et al., 2020a, 2018). Consequently, the introduction of ether functionalities into the cations of ionic liquids seems to be mainly a powerful tool to optimize the transport properties of ionic liquids by speeding up the dynamics on molecular scale near or below ambient temperature.

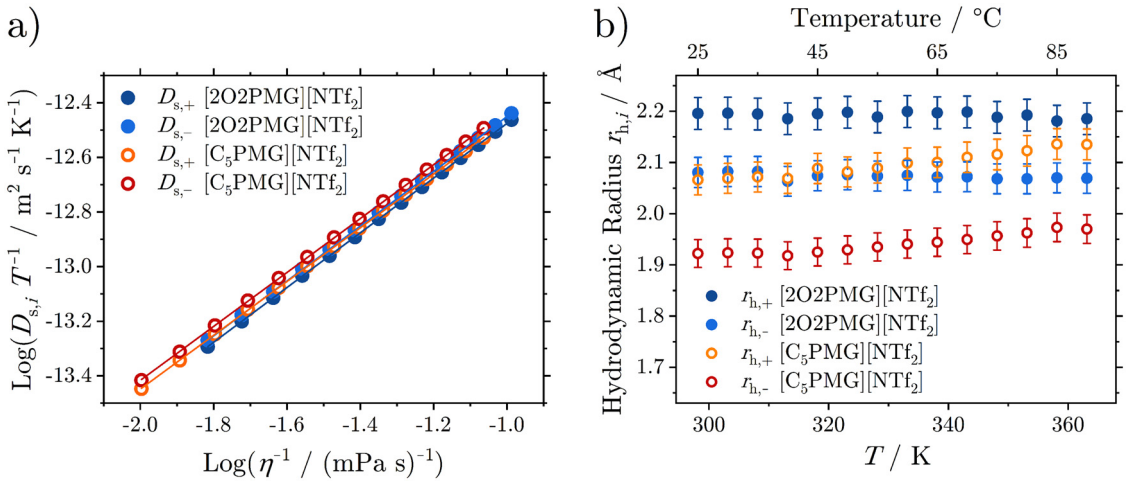

Fig. 4. (a) Stokes–Einstein(–Sutherland) plot for the $[NTf_2]^-$ ionic liquids. (b) Calculated hydrodynamic radii for the ionic liquid ions at different temperatures assuming the Stokes–Einstein Eq. (8) for stick conditions ($f = 6\pi$).

The reciprocal Haven ratios of both ionic liquids show a slight decline when the temperature is elevated, Fig 3d. This decrease in H_R^{-1} is somewhat non-linear and flattens with higher T being 0.582 in the case of [2O2PMG][NTf_2] and 0.595 for [C_5PMG][NTf_2] at 90 °C. A slight decrease in H_R^{-1} is also found for other ionic liquids classes (Rauber et al., 2018; Nordness and Brennecke, 2020). As the origin of the discrepancy between the Nernst–Einstein conductivity and the experimental conductivity is still unclear, the reason for this T-dependence also remains speculative. Nevertheless, the experimental investigation of these structure-property relations for different classes of ionic liquids might help to gain insight into the underlying mechanism.

The correlation between self-diffusion coefficients and viscosity is important to understand the peculiarities of the ionic fluids, similar to the interrelation between self-diffusion coefficients and observed conductivity. One important classical relationship is the Stokes–Einstein Eq. (8)

$$D_{s,i} = \frac{k_B T}{f \eta r_{h,i}} \tag{8}$$

with a friction factor f and the hydrodynamic radius $r_{h,i}$ of the moving spherically approximated species. The friction factor depends on the hydrodynamic boundary conditions (4π for slip and 6π for stick conditions) (Schmidt and Skinner, 2003). Consequently the T-dependent experimental viscosities and self-diffusion coefficients are interrelated by

$$\frac{D_{s,i}}{T} \propto \left(\eta^{-1}\right)^u \tag{9}$$

with u being a fractional exponent close to unity (Harris, 2016). The Stokes–Einstein(–Sutherland) plots of the investigated $[NTf_2]^-$ ionic liquids are shown in Fig. 4a. Fitting showed excellent linearity with values for u from 0.984 to 1.003. Details of the fitting are given in the supporting information.

The Stokes–Einstein relation (7) can be used to quantify the deviation of the individual ion from the hydrodynamic prediction. As there are two unknowns – the friction factor and the hydrodynamic radius – this can be done by calculating the friction factor for a presumed radius or by comparing the obtained calculated hydrodynamic radius for a defined friction factor with the assumed radii, for instance obtained by *ab initio* calculations. The T-dependent progression of the $r_{h,i}$ values assuming stick conditions ($f = 6\pi$) are shown in Fig. 4b. For the ether substituted ionic liquids the values remain constant in the investigated temperature range, while for the pentyl sample, [C_5PMG][NTf_2], a slight increase with T is observed. All the calculated hydrodynamic radii are significantly smaller than the ion radii obtained by *ab initio* calculations (radii $r_{ab\ initio,\ i}$ are 4.069 Å for $[2O2PMG]^+$, 4.124 for $[C_5PMG]^+$ and 3.686 Å for $[NTf_2]^-$). However, the trend of the cations being larger than the anion is well represented. For the [2O2PMG][NTf_2] sample the hydrodynamic radii of the anions are larger than the ones for [C_5PMG][NTf_2] (2.08 Å *vs.* 1.92–1.97 Å), which is probably the result of the more spherical geometry of the former ones (see Section 3.3). The differences between the calculated ion $r_{ab\ initio,\ i}$ and the ones calculated by the Stokes–Einstein Eq. (8) are comparatively large, ranging from 0.501 to 0.565. The details for the deviation of the correction factor when assuming that the hydrodynamic radius is equal to $r_{ab\ initio,\ i}$ are given in the supporting information. The strong deviations of the different radii might have their origin in the assumptions made in the derivation of the Stokes–Einstein relation (7), where spherical particles of larger size than the continuous medium in which it diffuses and negligible interactions are presumed. These assumptions are obviously not met in ionic liquids, where ions of similar size, strong Coulombic interactions and non-continuous, shell-like organizations of the ions are found. Strong deviation in the two methods for determining the ion radii seem to be a general finding for ionic liquids (Rauber et al., 2021a; Tokuda et al., 2005; Green et al., 2017) and may indicate the non-applicability of classical hydrodynamic theories, as the criteria used in the deviation of these are not met for ionic liquids (Cashen et al., 2022; Köddermann et al., 2008).

Cation conformations, liquid structure and rotational dynamics

Single crystal structure

The structural information obtained from single crystal X-ray analysis is of great value for ionic liquids as it allows a sophisticated picture of ion conformation and interactions on the molecular scale. Although the results obtained from single crystal structure analysis are for a different state of matter, it can be assumed that the underlying inter- and intramolecular interactions remain somewhat similar in the liquid state and that only the spatial order is lost (Hayes et al., 2015; Philippi et al., 2020b). For ionic liquids, the single crystal structural analysis has also proved to be a powerful tool to obtain experimental information about minimum energy conformers, which can then be compared to the geometries found in the liquid state or *in silico* (Philippi et al., 2022a, 2020b). For the guanidinium ionic liquids investigated here the conformation of the side chains is of most interest. Pictures of the asymmetric units of the two cations $[2O2PMG]^+$ and $[C_5PMG]^+$ with the $[PF_6]^-$ anion are shown in Fig. 5.

In the ether substituted sample the side chain conformation shows a curled structure with the ether oxygen pointing towards the carbon of the guanidinium moiety. The ether side chain in [2O2PMG][PF_6] with

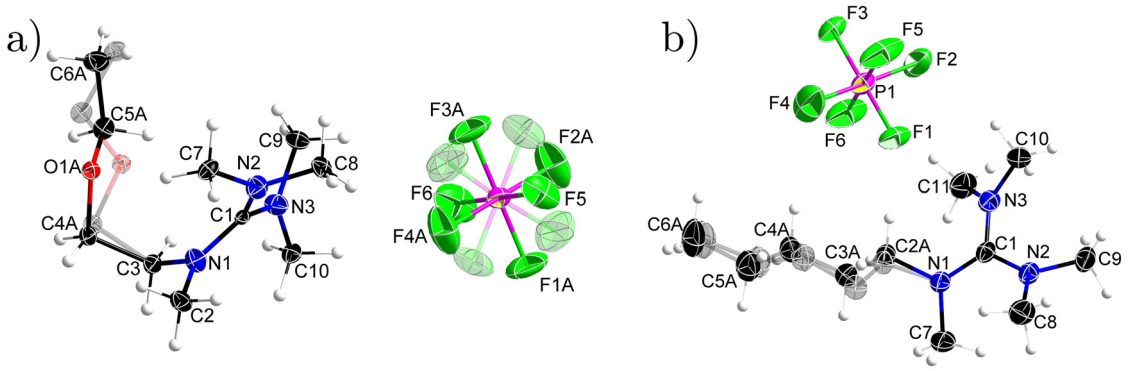

Fig. 5. Asymmetric unit of (a) the ether containing ionic liquid [2O2PMG][PF_6] and (b) the purely alkylated sample [C_5PMG][PF_6] as obtained by X-ray diffraction on single crystalline samples. Displacement ellipsoids are drawn at 50% probability level. The shaded atoms in the representations are the alignments with lower probability. In [2O2PMG][PF_6] the site occupancy factors of the shaded groups are approximately 7% in case of the ether side group and 11% for the fluorine atoms of the anion. For [C_5PMG][PF_6] the site occupancy factor of the shaded pentyl group is 21%. Color code: C black, N blue, O red, F green, P pink, H gray.

the highest site occupancy factors (0.928) has a dihedral angle ϕ_1(C–N–C–C) of –104.2 ± 0.2° or 255.8 ± 0.2°, and a dihedral angle ϕ_2(N–C–C–O) of 58.3 ± 0.3° starting from the nitrogen where the side chain is attached. For the side group with the lower site occupancy factors (0.072) the dihedral angles are ϕ_1(C–N–C–C) = –89.9 ± 2.2° or 270.1 ± 2.2° and ϕ_2(N–C–C–O) = 54.7 ± 3.3° The distance of the central guanidinium carbon to the oxygen with the highest site occupancy is 3.362 ± 0.003 Å, the distance to the oxygen with the lower population 2.917 ± 0.033 Å.

Contrary to the ether group the pentyl group adopts a linear conformation in the single crystal with the side chain pointing away from the cationic center. Thus, the functionalization has induced a change of the cation conformations with minimal effect on the cation mass. Torsion angles of the hydrocarbon chain with the highest site occupancy (0.787) are –121.8 ± 0.2° or 238.2 ± 0.2° for ϕ_1(C–N–C–C) starting from the center guanidinium carbon and –176.1 ± 0.2° or 183.9 ± 0.2° for ϕ_2(N–C–C–C) from the guanidium nitrogen. The side group with the lower site occupancy (0.213) has a torsion angle ϕ_1(C–N–C–C) of –109.1 ± 1.0° or 250.9 ± 1.0° combined with a torsion angle ϕ_2(N–C–C–C) of 168.5 ± 0.9°

These findings of the altered cation conformation in ionic liquids by exchanging the methylene group in γ-position with an oxygen finding are also reported for other ionic liquid cations, such as phosphonium or ammonium (Rauber et al., 2021a; Philippi et al., 2020a; Beckmann et al., 2022). Thereby the ether chain with the oxygen curls towards the cation center while in contrast the hydrocarbon chains adopt linear conformations pointing away from the cation center. This change in the cation conformation is also the reason for the accelerated dynamics of the ionic liquids with attached ether chains. On one hand the curled structure gives a more spherical shape to the cation which is beneficial for the dynamics. On the other hand, probably the more important factor, shielding of the cationic center by the polar ether group reduces interactions between cations and anions and thus changes the liquid structure (Rauber et al., 2021a; Beckmann et al., 2022). This altered cation conformation changes the enthalpic contributions slightly due to the better shielding of charges and increased cation-anion distances as well as the entropic contributions by allowing for diffuse ion configurations, increasing the configurational entropy of the liquids state (Rauber et al., 2021a). For protic tetramethyl guanidinium ionic liquids with 2-ethoxy-ethyl and pentyl chain substitution similar cation conformations of curled-ether and linear alkyl were found (Rauber et al., 2023).

Potential energy surface

Relaxed scans were performed from 0° to 360° in steps of 10° concomitantly for the two dihedrals ϕ_1 and ϕ_2 shown in Scheme 1 (Total of 37×37 = 1369 geometry optimizations with ϕ_1 and ϕ_2 frozen). The resulting potential energy surfaces of the ether and alkyl substituted pentamethyl guanidinium cations, including their minimum energy conformers, are show in Fig. 6. A threshold of 15 kJ mol^{-1} was chosen to identify the thermally accessible regions of the PES (dashed line). The geometries from single crystal structure measurements are also shown in Fig. 6, demonstrating the excellent agreement between gas phase *ab initio* calculations and solid-state bulk experiments.

The alkyl substituted pentamethyl guanidinium cation has more minima and a larger thermally accessible region with smaller barriers compared to the ether substituted cation. For $[C_4PMG]^+$, the energy of the three minima at $\phi_2 = 62°, 177°, 306°$ are within 2 kJ mol^{-1}, which is comparable to the accuracy of the theoretical method used. For the $[2O1PMG]^+$ cation, there is a clear preference for the $\phi_2 \neq 180°$.

Thus, the alkyl functionalized cation has a higher conformational flexibility both from entropic (number of minima) and dynamic (ease of transition between minima) viewpoints. This is in contrast to the common assumption that the favorable properties of ether functionalized ionic liquids stem from their high conformational flexibility (Tang et al., 2012). In line with our previous work on ether-functionalized cations, we observe pronounced curling of the ether functionalized side chain towards the positively charged core (Rauber et al., 2021a; Philippi et al., 2020a; Beckmann et al., 2022). The ether oxygen atom thus competes with the anions for coordination of the cation core (Kashyap et al., 2013; Yoshii et al., 2020; Shimizu et al., 2013). The intermolecular curling effectively shields the positive charge. The predominant underlying cause for this curling seems to be a combination of electrostatic and dispersion interactions of roughly equal strength, see supporting information.

Small-angle X-ray scattering

Information about the liquid structure of ionic liquids can be obtained by small-angle X-ray scattering (SAXS) (Hayes et al., 2015). The obtained scattering patterns usually contain up to three peaks in specific ranges of the scattering vector q. Higher q-ranges correspond to shorter distances in real space. Peaks at $q\ q\ > 1$ $Å^{-1}$ are thus usually interpreted as 'adjacency peaks' that result from various intra- and intermolecular contributions. The 'charge peaks' around $q = 0.8$ $Å^{-1}$ (Araque et al., 2015) stem from the shell-like organization of ionic liquids, where each ion is surrounded by countercharged ions. Due to cancellation of peaks and antipeaks this feature can be absent in the scattering patterns, which does not mean that there is no formation of ion cages in the liquid state (Araque et al., 2015; Kashyap et al., 2012). These charge peaks also correlate to the average ion distance in the liquids state. At smaller q values, 'polarity peaks' are found for some ionic liquids with longer non-polar parts (hydrocarbon or fluorocarbon chains) attached to the ions. This is mostly the case for cations with long alkyl tails and leads to the formation of a nanostructure consisting of non-polar hydrocarbon domains and polar, ionic regions. This polarity peak consequently has a higher

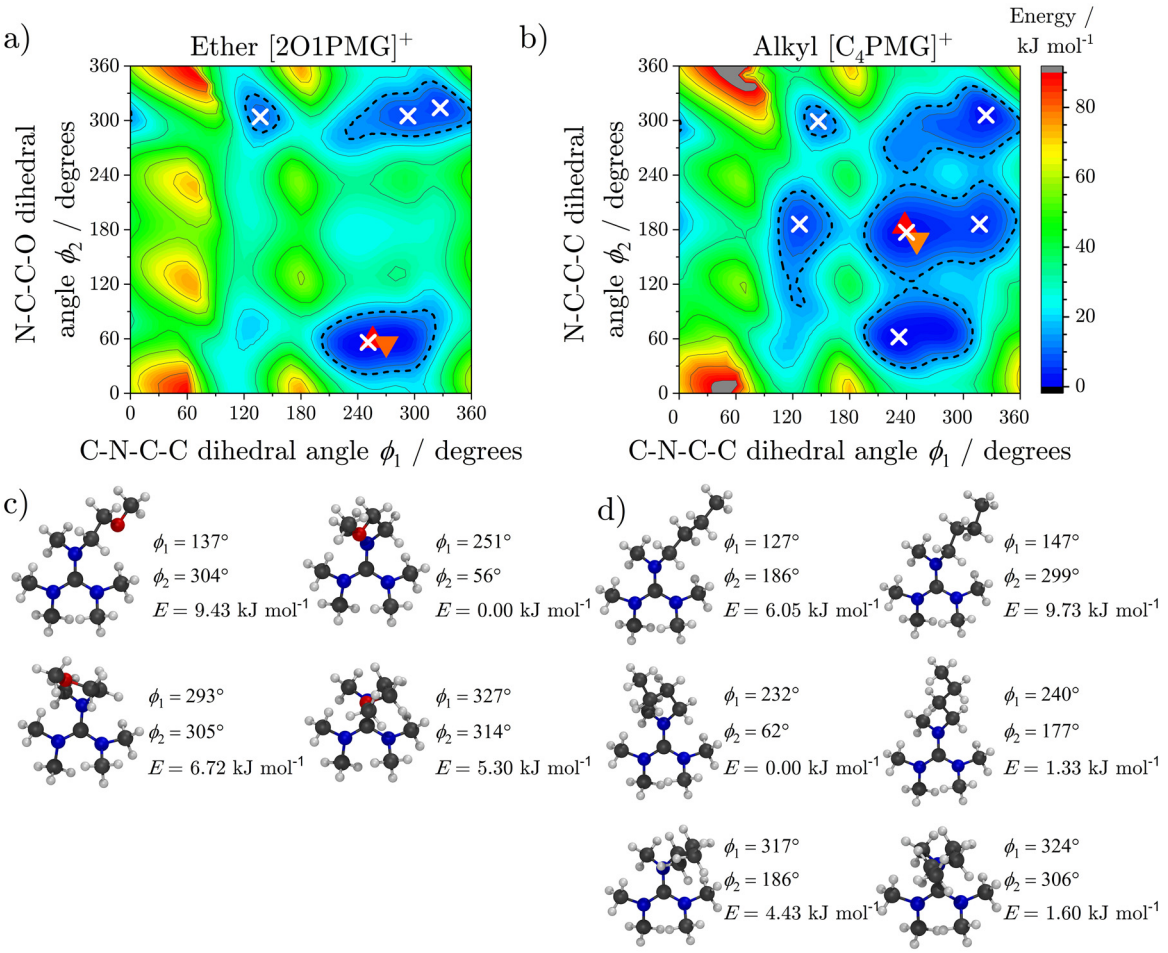

Fig. 6. Potential energy surfaces of the dihedral angle ϕ_1(C–N–C–C) *versus* (a) the dihedral angle ϕ_2(N–C–C–O) of the 2-methoxy-ethyl-pentamethyl guanidinium cation $[2O1PMG]^+$ cation and (b) the dihedral angle ϕ_2(N–C–C–C) of the methylene-substituted analogue butyl-pentamethyl guanidinium $[C_4PMG]^+$. The dashed lines represent the thermally accessible regions of the potential energy surface, assuming a barrier of 15 kJ mol^{-1} (Philippi et al., 2020b). The white crosses are the minimum energy structures of the potential energy surface and the triangles are the dihedral angles obtained from the singe crystal structure analysis (see Section 3.3.1). Red triangles with tip pointing upwards represent the cation conformations in the single crystal with the highest site occupation factor, orange ones with tip pointing downwards those with lower site occupation. Graphical representation of the minimum energy structures from the potential energy surfaces for (c) the $[2O1PMG]^+$ and d) the $[C_4PMG]^+$ cation with related dihedral angles and energies at the MP2/cc-pVTZ//B3LYP-GD3BJ/6-311+G(d,p) level of theory.

Table 5
Fitting parameters $D_{s,i,0}$, $B_{D_{s,i}}$ and $T_{0,\ D_{s,i}}$ following the VFT Eq. (3) for the self-diffusion coefficients $D_{s,i}$ (cation: i = +; anion: i = −) including Angell strength factor for the self-diffusion coefficients $\delta_{D_{s,i}}$ and activation energies $E_{a,D_{s,i}}^{25°C}$ for the self-diffusion at 25 °C. All coefficients of determination $R^2 \geq 0.99998$.

Ionic liquid	i	$D_{s,i,0}$ / 10^{-8} m^2 s^{-1}	$B_{D_{s,i}}$ / K	$T_{0,\ D_{s,i}}$ / K	$\delta_{D_{s,i}}$	$E_{a,D_{s,i}}^{25°C}$ / kJ mol^{-1}
[2O2PMG][NTf$_2$]	+	1.416 ± 0.08	−997.5 ± 22.9	152.2 ± 2.1	6.55 ± 0.17	40.0 ± 0.6
[2O2PMG][NTf$_2$]	−	1.306 ± 0.04	−832.5 ± 9.0	156.5 ± 1.1	6.06 ± 0.06	40.2 ± 0.6
[C$_5$PMG][NTF$_2$]	+	1.299 ± 0.04	−958.2 ± 11.4	163.3 ± 1.0	5.87 ± 0.08	46.7 ± 0.7
[C$_5$PMG][NTF$_2$]	−	1.422 ± 0.06	−959.9 ± 13.6	163.4 ± 1.2	5.88 ± 0.09	47.1 ± 0.6

intensity and is shifted to larger real-space distances in the case of pronounced nanostructuring that is typically caused by long alkyl groups (Hayes et al., 2015).

The experimental SAXS patterns of the guanidinium ionic liquids that could be obtained in liquid state at ambient temperature are shown in Fig. 7 and the obtained peaks of the scattering vectors q with the calculated real-space distances and ion distances from the *ab initio* radii are given in Table 6.

Weak polarity peaks are observed only for [2O2PMG][TFA] and [C$_5$PMG][NTf$_2$]. Only the samples with the [NTf$_2$]$^-$ and the [BETI]$^-$ anion have a clear charge peak. The ionic liquids with ether containing cation with the [FSI]$^-$, [NTf$_2$]$^-$ and [TFA]$^-$ anions show two adjacency peaks, whereas [2O2PMG][BETI] and [C$_5$PMG] [NTf$_2$] show only one peak at high q. The calculated real space distances of the ions (charge peak) are in good agreement with the sum of the radii from the *ab initio* calculation. For the ether cation the sum of the *ab initio* ion radii is approximately 0.5 Å smaller than the ion distances in the liquid for both the [NTf$_2$]$^-$ and the [BETI]$^-$ anion. The difference of 0.34 Å in the ion distance between the ionic liquids with the two different anions is in excellent agreement with the difference in the anion sizes of 0.345 Å from the *ab initio* calculations.

As polarity peaks and nanosegregation usually emerge for ionic liquids with groups equal to or longer than butyl for various cations (Hayes et al., 2015), it is not surprising that the guanidinium ionic liq-

Table 6
Peak positions of the scattering vector q and calculated real space distances.

Ionic liquids	Peak positions			Real space distance			$r_+ + r_-$ / Å
	Polarity / Å^{-1}	Charge / Å^{-1}	Adjacency / Å^{-1}	Polarity / Å	Charge / Å	Adjacency / Å	
[2O2PMG][FSI]	—	—	1.08; 1.63	—	—	5.80; 3.85	7.31
[2O2PMG][NTf$_2$]	—	0.76	1.04; 1.42	—	8.25	6.06; 4.43	7.76
[2O2PMG][BETI]	—	0.73	1.09	–	8.59	5.79	8.10
[2O2PMG][TFA]	0.49	—	1.13, 1.56	12.8	—	5.54; 4.02	6.95
[C$_5$PMG][NTf$_2$]	0.45	0.80	1.18	13.8	7.86	5.33	7.81

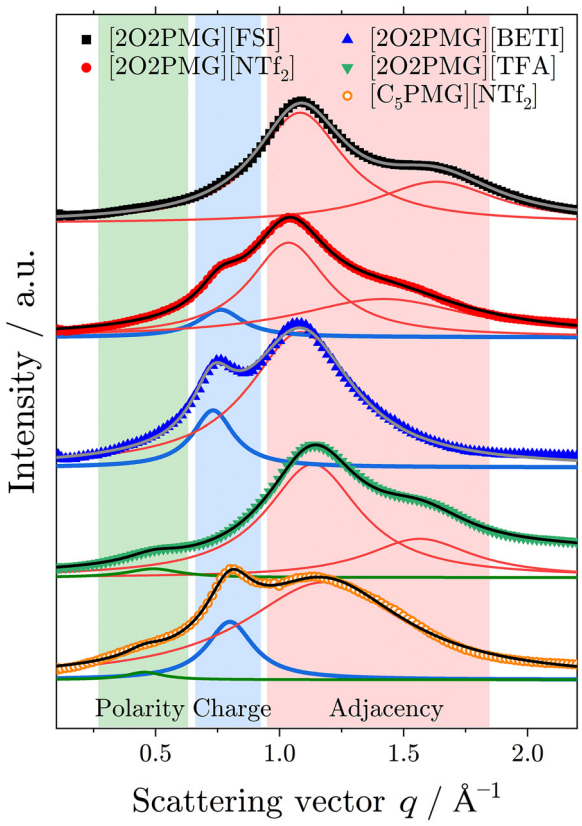

Fig. 7. Small-angle X-ray scattering patterns of the investigated guanidinium ionic liquids at 25 °C. Colors in the background show the regions where polarity, charge and adjacency peaks are found. Drawn lines are the peak fits using Lorentzian functions with the colors indicating the type of peak (from the q range in which they are located).

uid with the pentyl chain also shows this signature. The distance of the nonpolar domains is slightly larger than the characteristic domain size of the 1-methyl-3-pentyl-imidazolium cation $[C_5C_1im]^+$ with the $[NTf_2]^-$ anion, which has been reported to be 11.0 Å (Russina et al., 2009). This greater distance for the pentyl-pentamethyl guanidinium can be simply rationalized by the larger size of the guanidinium moiety. The absence of nanosegregation in ionic liquids with ether tails is the result of the altered cation conformation. While the hydrocarbon chain in the guanidinium ionic liquid adopts a linear conformation, similar to other ionic liquid cation classes, the ether chain curls toward the cation center. This cation conformation of the ether-substituted guanidinium prevents the formation of nonpolar microdomains and shields the positive charge of the cation center, which has also shown to be the case for other types of ionic liquid cations (Rauber et al., 2021a; Philippi et al., 2020a; Amith et al., 2022). The polarity peak of [2O2PMG][TFA] might be attributed to the higher basicity of this particular anion which is competing with the ether chain for the positively charged cation center. A similar observation was also made for ether-substituted ammonium ionic liquids with the trifluoroacetate anion (Rauber et al., 2021a).

The occurrence of two adjacency peaks in ionic liquids is a quite rare observation and has only been, to the best of our knowledge, reported for ionic liquids with the tricyanomethanide $[C(CN)_3]^-$ and tetracyanoborate anions $[B(CN)_4]^-$ (Philippi et al., 2020a; Dhungana et al., 2016). The occurrence of two adjacency peaks has been rationalized by the shift of the intermolecular contributions of the cations to the adjacency correlations towards lower q values as a result of anion sizes changing the ion arrangements. In this set of guanidinium ionic liquids the incidence of the two adjacency peaks might also be attributed to the ion size, as for the ether ionic liquids a single adjacency peak is only found for the $[BETI]^-$ anion, which is the largest in this set.

Nuclear magnetic resonance spectroscopy

For a deeper understanding of the obtained cation conformation and the rotational dynamics in the liquids state, we investigated the pure ionic liquids nuclear magnetic resonance (NMR) spectroscopy at different temperatures.

Variable temperature NMR on [2O2PMG][NTf$_2$]. From the single crystal X-ray structure analysis as well as the potential energy surface calculations, a curled structure of the $[2O2PMG]^+$ cation with the ether side chain in the liquid state is to be expected. However, due to partial double bond character of the C–N bonds in the guanidinium cation center, restricted rotations for the hexaalkyl-substituted guanidinium ionic liquids are also anticipated (Moscardini et al., 2019). A stacked-plot of the temperature-dependent ^{1}H-NMR spectra is shown in Fig. 8a.

In the temperature-dependent spectra, a clear difference in the low and high T region is found. At lower temperatures, the spectra contain more peaks which merge into each other at medium T, resulting in the observed high T spectra with fewer resonances. Spectra showing the methylene protons in the side chain at different temperatures are given in Fig. 8b, while the section of the methyl groups attached to the guanidinium unit is shown in Fig. 8c. Differences in the spectra at different temperatures can be attributed to the slow rotation around the partial double bonds in the guanidinium center. In total, there are three different bonds of central guanidinium carbon to the nitrogen atoms that are restricted in their rotation. These are the two C–N$(CH_3)_2$ bonds, which can be seen by the four unequal $N(CH_3)_2$ groups, and the C–N(2O2)CH_3 bond, which causes the splitting of the protons in the α and β positions of the ether side chain (sketched in Fig. 8a). In addition, the restricted motion of the N–C_α and C_α–C_β causes the particular splitting patterns of the protons attached to these carbons. At lower temperatures some protons are observed as individual resonances since these protons remain in different chemical environments for longer times due to slow

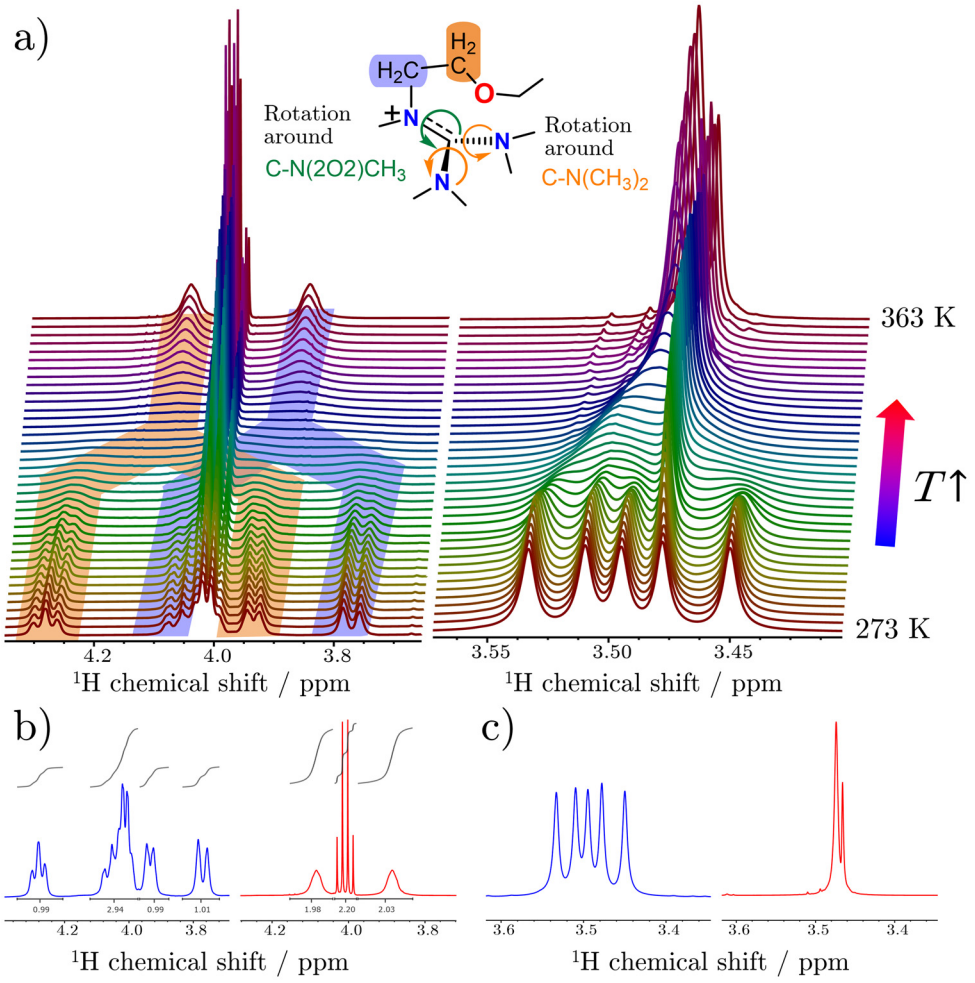

Fig. 8. (a) Overview of the T-dependent ^{1}H-NMR spectra of [2O2PMG][NTf_2] as stacked plot (at 500 MHz, referred to external $(CDCl_2)_2$). The progression of the hydrogen nuclei in the ether side chain is highlighted with color (orange = N–CH_2–**CH_2**–O; violet = N–**CH_2**). The sketch shows the guanidinium C–N bonds with restricted rotations causing the splitting of the signals. (b) Excerpt of the NMR spectra showing the protons in α, β and δ position to the guanidinium nitrogen at 273 K (blue) and 363 K (red). Detailed multiplicity analysis and assignment of the hydrogen atoms in the cation conformation is given in Table S20 and Fig. 9. (c) Signal splitting of the methyl groups at 273 K (blue) and 363 K (red). Five individual peaks are visible at lower temperature, while at higher T two peaks appear in a ratio of 4:1, corresponding to the protons of $C(N(CH_3)_2)_2$ and $N(2O2)CH_3$.

rotations. Signal splitting in the NMR spectra due to slow rotations is observed when the rate constant of rotation k_{rot} is much slower than the differences in the chemical shifts $\Delta\nu$ of the signals, so $k_{rot} \ll \Delta\nu$. As the available thermal energy increases, these restricted motions become faster, leading to the coalescence of the formerly separated peaks and the appearance of a single resonance at higher temperatures, when $k_{rot} \gg \Delta\nu$. The different chemical shifts, their multiplicities, coupling constants and assignments at 273 K and 363 K are given in Table S20 of the supporting information, the spectral ranges and line fittings of the ^{1}H NMR signals of the 2-ethoxy-ethyl group are shown in Fig. 9c for the lower temperature (273 K) and in Fig. S12 for the high T (363 K). Due to the characteristic chemical shifts and splitting patterns, the peaks at low temperatures can be assigned to the different protons, showing that the conformation of the cation in the liquid state is the same as in the solid state and is the minimum energy conformation as predicted from the *ab initio* calculations.

At lower temperatures with slow rotations around the C–N bonds ($k_{rot} \ll \Delta\nu$) the ^{1}H-NMR peaks can be assigned when considering the minimum energy geometry from the *ab initio* calculations (which in turn is close to the situation in the solid state, see Section 3.3.1), although a shorter side chain was chosen as a model system. Signals of the five methyl groups attached to the guanidinium center are well separated, located at 3.4 to 3.6 ppm, see Fig. 8a. The resonance of the side-chain methyl group is at 1.68 ppm showing a triplet with a coupling constant $^3J_{HH}$ of 7 Hz, Fig. 9c. In addition, the protons of the methylene unit in δ position to the guanidinium nitrogen can be assigned to the quartet located at 4.01 ppm indicating a free rotation of the O–CH_2(CH_3) bond. However, at lower temperatures this quartet is overlapped by the signal from a single proton from the α position, see Fig. 9c. The four remaining signals all have the same integral (of one proton per signal, see Fig. 8b and can be attributed to the remaining hydrogen atoms in α and β position of the ether side group. To understand the splitting of the ^{1}H-NMR resonances of these methylene units, it is helpful to assume the minimum energy conformation from the solid state and/or the computations, which has the dihedral angles ϕ_1(C–N–C–C) of 251° and ϕ_2(N–C–C–O) of 56°. The conformation of the hydrogen atoms in the α and β positions of the side chain is shown in Fig. 9a and b in schematic representations.

The spectra at 273 K show two triplets and two doublets. Attribution of the signals to the protons can be made from the splitting patterns and strength of the of $^2J_{HH}$ geminal and $^3J_{HH}$ vicinal coupling constants. Geminal couplings can reach up to 12 Hz in comparable systems with N- and O-substituents. Vicinal couplings are the result of different overlaps of molecular orbitals (Karplus, 1963). Their magnitude depends on the dihedral angle of the two coupling protons and is well described by the Karplus equation (Hunter et al., 2005). Here, the coupling constants range between 10 and 12 Hz for antiperiplanar (dihedral angle is 180°) and 2–3 Hz for gauche rotamers (dihedral angle is 60°).

Each of the two methylene groups in α and β position to the guanidinium N has one proton in gauche position (H_B and H_C, respectively) to the two neighboring methylene group protons and a proton (H_A and H_D, respectively), which has both an antiperiplanar and a gauche position to a vicinal proton, see Fig. 9c. Utilizing Heteronuclear Single Quantum Coherence (HSQC) NMR spectroscopy for the correlation of ^{1}H and ^{13}C nuclei allows the assignment of the proton signals to a carbon of the molecular structure (see supporting information). This re-

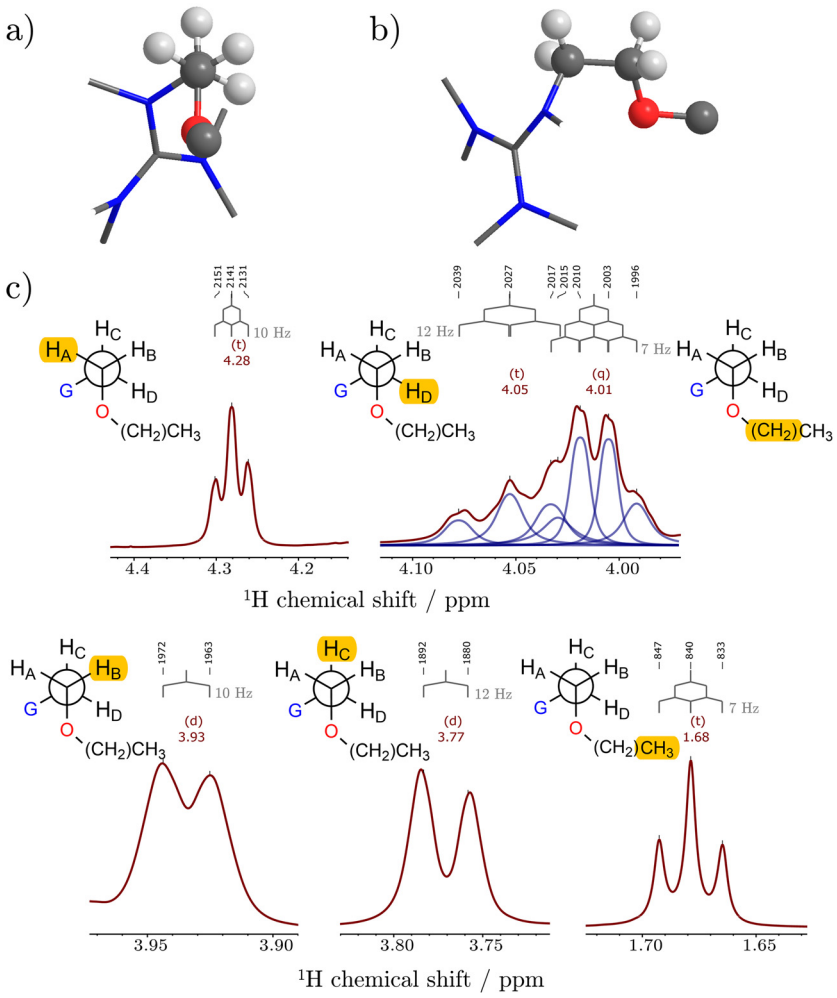

Fig. 9. Schematic representation of the minimum energy conformer obtained from the calculation of the potential energy surface for the $[2O1PMG]^+$cation (ϕ_1(C–N–C–C) of 251° and ϕ_2(N–C–C–O) of 56°). The geometric arrangement of hydrogen atom of the side chain in α and β position is shown in (a) with the C_α–C_β bond perpendicular to the paper plane and (b) in the paper plane, respectively. (c) The individual multiplets of the 2-ethoxy-ethyl side chain in the ^{1}H-NMR(500 MHz, referred to external $(CDCl_2)_2$) spectra at 273 K with line shape analysis and assignment to the molecular structure of one of the two equivalent rotamers with the ether atom being in gauche position to the guanidinium moiety. Fitted peaks are shown in blue.

veals that the protons at 3.93 and 4.28 ppm belong to the carbon in β-position (H_A and H_B) and the ones at 3.77 and 4.05 ppm (H_C and H_D) to the methylene group next to the guanidinium nitrogen. For the sample [2O2PMG][NTf_2] the occurrence of these individual proton signals at lower T reveals the persistent cation conformation due to the coordination of the ether-oxygen towards the guanidium carbon. This significantly slows down the rotations around the C–N(2O2)CH_3, C–N$(CH_3)_2$ bonds as well as the N–C_α bond and C_α–C_β of the ether side chain, while a free rotation is only possible for the bonds of the ethoxy group (O–C_δ and C_δ–C_ϵ). Due to the slow rotation a locked conformation is observed by NMR spectroscopy in the pure, liquid state, similar to the situation in the crystal. This locked conformation consists of two chemically equivalent rotamers (of which only one is shown in Fig. 9c with the ether atom being in gauche position to the guanidinium moiety with respect to the C_α–C_β bond. Since the geminal and the antiperiplanar vicinal coupling constants are large and almost equal in magnitude and the gauche couplings are small and unresolved in the low temperature spectra, H_A and H_D appear as broad triplets and H_B and H_C as broad doublets, as shown in Fig. 9c and Table S20.

At higher temperatures, the rotation around the C-N bonds is significantly faster ($k_{rot} \gg \Delta\nu$) so that it is not possible to resolve the individual rotamers in the used frequency range (in this case 500 MHz). Consequently, the signals of the individual protons in the side chains are observed as a single resonance. In this case the methylene groups in the α and β positions to the guanidinium nitrogen are then observed as triplets which each integrate for two protons, due to the fast rotations. The individual signals of the protons in the ether side chain at 363 K together with their assignment are shown in Fig. S12. All multiplets of the side chain are separated from each other. The broadened triplets of the α and β methylene groups and guanidinium methyl groups indicate that the rotation around the N–C_α bond and C_α–C_β bond is still comparatively slow, although no individual rotameric peaks for the vicinal couplings are observed at higher T. This indicates that the coordinating ether chain conformation, slowing down the molecular rotations in the ionic liquid cation, is still persistent at elevated temperatures. This is also in accordance with the constant hydrodynamic radius that would be expected to change if the ion conformation changed significantly.

Variable temperature NMR on [C_5PMG][NTf_2]. For the [C_5PMG][NTf_2] the individual T-dependent ^{1}H-NMRs are shown in Fig. 10a. The full plot is given in the supporting information. Similar to the ether substituted sample there is a splitting of some proton signals at lower temperatures. On the one hand the restricted rotation of the C–N$(C_5H_{11})CH_3$ bond causes a splitting of the methylene protons in the α and β beta positions, Fig. 10b and d, and on the other hand the restricted rotations of the C–N$(CH_3)_2$ bonds cause a broadened and asymmetric peak of these methylene group resonances, see Fig. 10c. At lower temperatures the protons of the α and β methylene groups appear as broad singlets rather than sharp multiplets, as it would be the case for fast rotations ($k_{rot} \gg \Delta\nu$) around the C–N$(C_5H_{11})CH_3$ bond. This is especially true for the two protons of the β methylene group that form two separated broad peaks at 263 K, but as a quintet at 363 K, see Fig. 10d. Combined with the finding that the signals from the methyl group α to the nitrogen shows a clear, much less broadened triplet at higher temperatures it can be concluded that the rotation around the C–N$(C_5H_{11})CH_3$ bond is

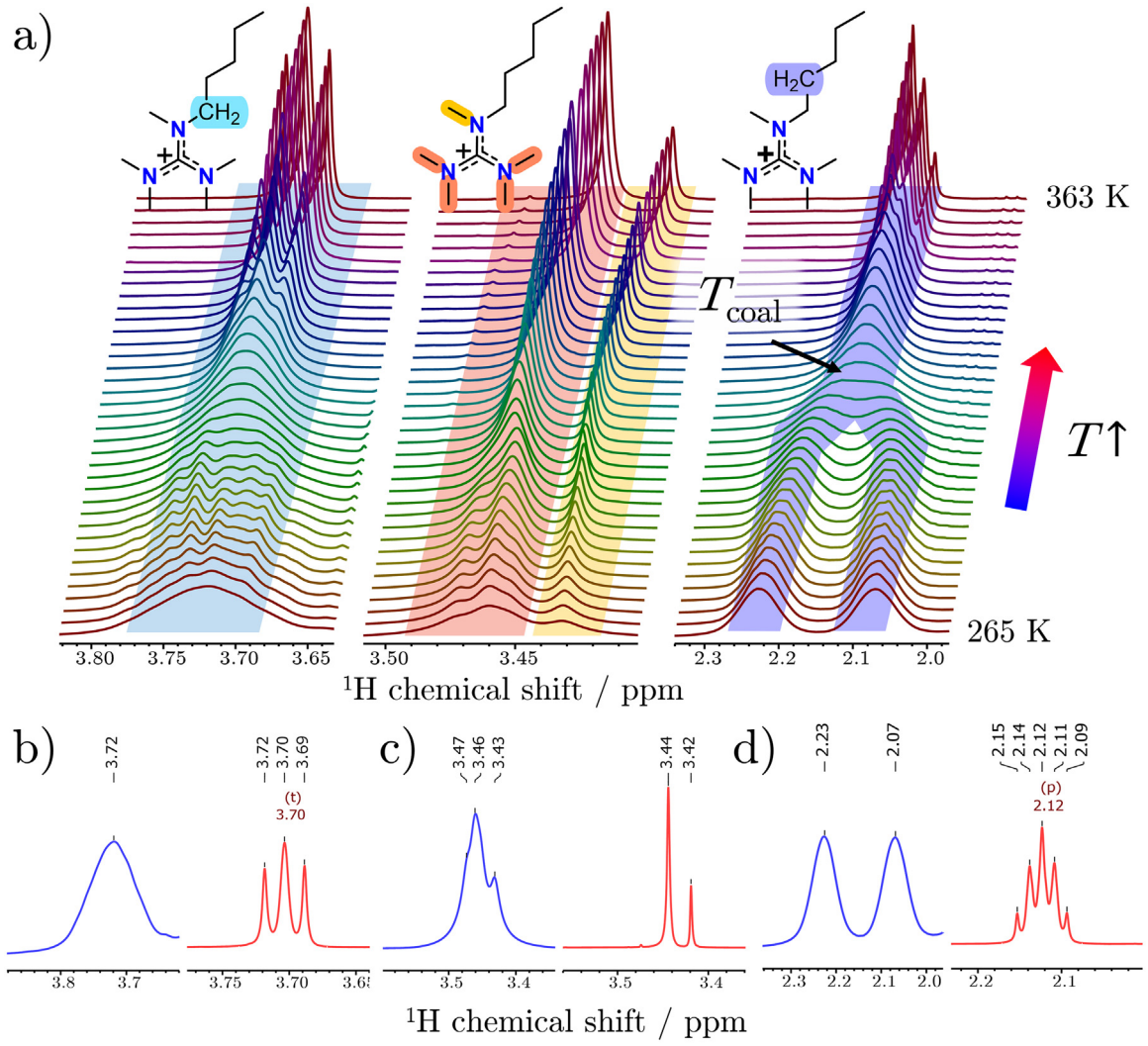

Fig. 10. (a) Stacked plot of the variable temperature ^{1}H-NMR (500 MHz, referred to external $(CDCl_2)_2$) measurements for the signals changing their shape/coalescence with increasing T. Spectra of the protons for (b) the methylene group in α position to the guanidinium nitrogen, (c) the methyl groups at the guanidinium moiety and (d) the methylene group β to the N. The blue spectra are recorded at 265 K and the red ones at 363 K.

much less restricted than when the side chain contains the ether. This again shows the altered cation conformation of the $[2O2PMG]^+$ cation and the influence of the ether side chain on the rotational dynamics of the bond in the cation.

3.4. Rotational dynamics

Temperature-dependent NMR spectroscopic measurements can be used to obtain kinetic data about rotational processes, if the processes have sufficient rate constants / time scales. The analysis of the coalescence temperature T_{coal} at which peaks in the spectrum merge, and the analysis of the line shape at this temperature can be used to determine the rate constant of the rotation at the coalescence temperature k_{coal}. For T_{coal} this can be done using the approximation in Eq. (10)

$$W_{1/2} = \Delta\upsilon_0 = \sqrt{2}\pi^{-1}k_{coal} \tag{10}$$

with $W_{1/2}$ is the peak width at half height of the signal at the coalescence temperature and $\Delta\upsilon_0$ the frequency difference in absence of an exchange (the peak separation at low temperatures given in Hz, where the rotations are slow) (Gutowsky and Cheng, 1975; Foreiter et al., 2014; Modarresi-Alam et al., 2007). From the rotational rate constant at the coalescence temperature k_{coal} the Gibbs free energy $\Delta G^{\neq}_{coal}$ of the rotational barrier (activation energy of the rotation) can be calculated using the Eyring-Eq. (11) in the form

$$\Delta G^{\neq}_{coal} = -RT_{coal}\ln\left(\frac{k_B T_{coal}}{h k_{coal}}\right) \tag{11}$$

with the Boltzmann constant k_B and the Planck constant h. The values obtained for the different rotational barriers at the stated coalescence temperatures are given in Table 7.

All values for the rotational barriers are quite close to each other, presumably as a result of the comparatively small T-range and the structural similarities of the cations. However, the rotational barriers of the ether containing ionic liquids are higher than for the purely alkylated sample. This is not surprising, since the cation conformation with the curled ether chains restricts the rotational motion of the bonds in the ether-cation, especially the C–N(2O2)CH_3 bond (and the N–C_α plus C_α–C_β bonds, see above). For the hexamethyl guanidinium cation in deuterium oxide rotational barriers of 64.9 kJ mol^{-1} are given in the literature (Dietrich et al., 1980). A pentamethyl guanidinium cation with a large substituent in 1,1,2,2-tetrachloroethane-d_2 showed rotational barriers for the C–N$(CH_3)_2$ bond of 64 kJ mol^{-1} with a comparable T_{coal} value of 324 K (Butschies et al., 2010). Such close values of the different guanidiniums in the pure state and solvent indicate that the rotations in the cations are influenced only slightly affected by the length of the substituents and the surrounding media. Rotational barriers of

Table 7
Coalescence temperatures T_{coal} for the different resonances of the investigated ionic liquids. The separation of the resonances at low temperatures $\Delta\upsilon_0$, and the width of the peaks at the coalescence temperature $W_{1/2}$ were used to calculate the rate constant of the rotation at the coalescence temperature k_{coal} and the Gibbs free energy of activation for the rotation at this temperature $\Delta G^{\ddagger}_{coal}$.

Ionic liquid	Protons	T_{coal} / K	$\Delta\upsilon_0$ / Hz	$W_{1/2}$ / Hz	k_{coal} / Hz	$\Delta G^{\ddagger}_{coal}$ / kJ mol^{-1}
[2O2PMG][NTf$_2$]	N–CH$_2$–**CH$_2$**	330.7	174.1 ± 2.0	—	386.7 ± 4.4	64.8 ± 1.1
	N–**CH$_2$**	328.2	141.7 ± 2.0	—	314.1 ± 4.4	64.9 ± 1.1
	N(**CH$_3$**)$_2$	305.7	—	14.8 ± 3.0	32.9 ± 6.6	66.6 ± 1.6
	N(**CH$_3$**)$_2$	315.7	—	30.1 ± 3.0	66.9 ± 6.6	66.4 ± 1.6
	N(**CH$_3$**)$_2$	315.7	41.5 ± 1.0	—	92.5 ± 4.4	65.6 ± 1.1
[C$_5$PMG][NTf$_2$]	N–CH$_2$–**CH$_2$**	313.3	78.8 ± 2.0	—	175.0 ± 4.4	63.3 ± 1.1
	N–CH$_2$–**CH$_2$**	313.3	—	71.0 ± 2.0	157.6 ± 4.4	63.6 ± 1.1

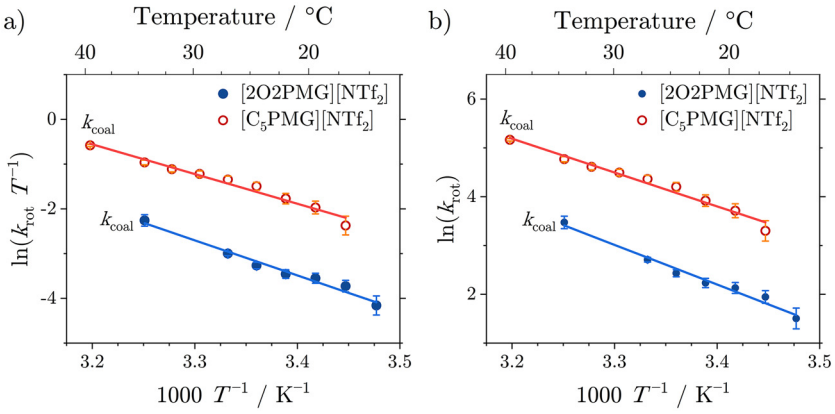

Fig. 11. (a) Eyring and (b) Arrhenius plot for the determination of the thermodynamic parameters of the C–N(X)CH$_3$ bonds' (X = 2O2 or C$_5$H$_{11}$) rotational dynamics. Values for the rate constant of rotation k_{rot} are obtained from for the signals of the methylene group in β-position to the guanidinium nitrogen.

78.7 kJ mol^{-1} around the imine bond have been published for the corresponding non-ionic pentamethyl guanidine (Bauer et al., 1968), indicating that the delocalization of the π-electrons plays an important role in the activation of the rotation for the guanidinium ionic liquids. *Ab initio* calculations for a tetramethyl guanidinium cation with a cyclic pentyl chain gave a slightly higher conformational barriers of 67.3 kJ mol^{-1} for the rotation of the C–N(CH$_3$)$_2$ (Moscardini et al., 2019). Similar values for rotational barriers of approximately 64 kJ mol^{-1} have been reported for neat chiral thiouronium ionic liquids with the [NTf$_2$]$^-$ anion (Foreiter et al., 2014).

For temperatures below the coalescence with slow exchange, the rate constant of the rotation can be obtained by the change in peak separation according to Eq. (12) (Gasparro and Kolodny, 1977).

$$k_{rot} = \frac{\pi}{\sqrt{2}}\left(\Delta\upsilon_0^2 - \Delta\upsilon_e^2\right)^{1/2} \tag{12}$$

with $\Delta\upsilon_e$ the separation of the peaks (in Hz) when slow exchange is present. Rate constants of the rotational dynamics of the C–N(X)CH$_3$ (with X = 2O2 or C$_5$H$_{11}$) bond are determined by the methylene groups in the β-position of the side chains. In both samples these signals show a sufficient separation and are not overlapped. From the temperature-dependence of the rotational constants of the activation enthalpy $\Delta H^{\ddagger}_{rot}$ and activation entropy $\Delta S^{\ddagger}_{rot}$ of the rotational process can be obtained by the Eyring Eq. (13) in the form

$$k_{rot} = \frac{\kappa k_B T}{h}\exp\left(\frac{\Delta S^{\ddagger}_{rot}}{R}\right)\exp\left(\frac{\Delta H^{\ddagger}_{rot}}{RT}\right) \tag{13}$$

assuming a transmission coefficient κ of unity, due to the intramolecular nature of the rotational process (Guerra et al., 2020). The Eyring plots of $\ln(k_{rot}\,T^{-1})$ *vs.* T^{-1} with the determined rate constants for the rotation around the C–N(X)CH$_3$ bond of the guanidinium moiety are given in Fig. 11a. The resulting activation parameters from the Eyring Eq. (13) are given in Table 8. Similar to other rate constants or the transport properties it is possible to obtain the activation energy of the rotation $E_{a,\,rot}$ by the Arrhenius Eq. (4). The resulting Arrhenius plot

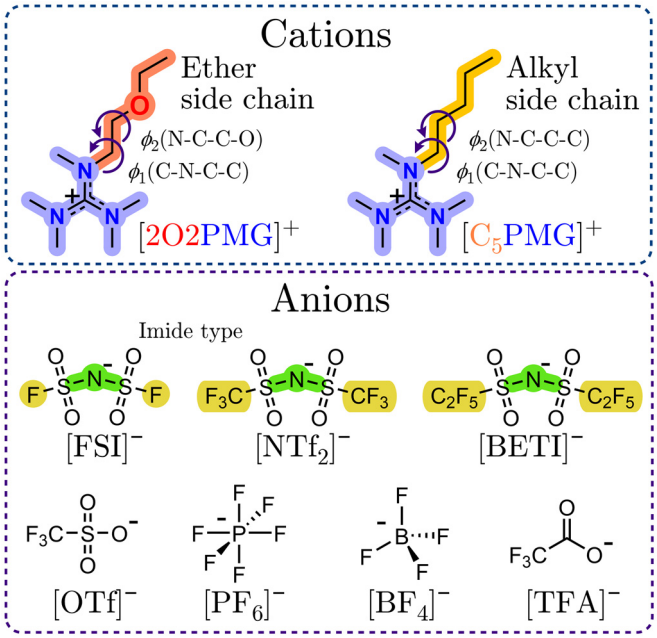

Scheme 1. Molecular structures and abbreviations of the investigated cations and anions forming the pentamethyl guanidinium ionic liquids. Furthermore, the dihedral angles ϕ_1 and ϕ_2 of the bonds in the side chain, which were used for the construction of the potential energy surfaces, are illustrated.

($\ln(k_{rot})$ *vs.* T^{-1}) is show in Fig. 11b and the values for $E_{a,\,rot}$ are given in Table 8.

The results from the Eyring plot show a significantly higher enthalpy of activation for the conformational rotational process around the C–N bond of the guanidinium moiety for the ether substituted ionic liquid.

Table 8
Activation enthalpy $\Delta H^{\ddagger}_{rot}$ and activation entropy for the $\Delta S^{\ddagger}_{rot}$ from the Eyring Eq. (13) as well as activation energy from Arrhenius Eq. (4) for the rotation around the C–N(X)CH_3 bond (X = 2O2 or C_5H_{11}) for the samples with ether chain and pentyl group.

Ionic liquid	$\Delta H^{\ddagger}_{rot}$ / kJ mol^{-1}	$\Delta S^{\ddagger}_{rot}$ / J mol^{-1} K^{-1}	$E_{a,\ rot}$ / kJ mol^{-1}
[2O2PMG][NTf_2]	65.1 ± 4.2	73.5 ± 15.4	67.5 ± 4.2
[C_5PMG][NTf_2]	55.2 ± 3.5	25.3 ± 11.6	57.6 ± 3.5

This indicates that the interactions of the oxygen in the ether chain with the carbon of the guanidinium center (as shown above) hinders the rotation of the C–N bond at which the ether chain is attached. A similar result is also obtained when using the Arrhenius activation energy. Upon substitution of the γ-methylene group in the pentyl chain with an oxygen atom the activation energy of the rotational process increases significantly as a result of the intramolecular coordination.

Conclusion

In this contribution we presented the synthesis and characterization of a set of novel pentamethyl guanidinium ionic liquids with the 2-ethoxy-ethyl side group and various anions commonly used in ionic liquids. The guanidinium cation constitutes an interesting cation subclass of ionic liquids with attractive properties that lacks detailed insights due to their commercial non-availability. The results for [2O2PMG][NTf_2] was compared to the isostructural guanidinium ionic liquids where the ether functionality was replaced by a methylene group. We measured the thermal properties and density as well as the transport properties viscosity, conductivity and diffusivity of the samples in dependence of temperature. Contrary to ionic liquids based on other cation-types the ether functionalization seems to stabilize the crystalline state. The ionic liquids with imide-type anions can be obtained in liquid state at ambient temperatures and show good transport properties that are comparable to those of other established cations, such as imidazolium or ammonium. Using single crystal structure analysis, *ab initio* calculations, and variable temperature nuclear magnetic resonance spectroscopy we were able to show that the ether-substituted samples have an altered cation geometry compared to the samples with only hydrocarbon groups in both solid and liquid state. The ionic liquids with the ether group adopt a more compact, curled structure with the oxygen atom coordinating towards the central carbon of the guanidinium, whereas the ions with the pentyl group show a linear conformation. Furthermore, we were able to determine the rate constants of the rotation from variable temperature nuclear magnetic resonance measurements. The Eyring equation revealed that the rotation of the carbon-nitrogen bond with the attached side chain has a higher activation enthalpy for the ether side group than the pentyl side chain. This enthalpic contribution is the result of the persistent coordination of the ether chain towards the positively charged cation center on NMR timescales.

Declaration of Competing Interest

The authors declare that they have no known competing financial interests or personal relationships that could have appeared to influence the work reported in this paper.

Data availability

Experimental data values and computational results are given in the supporting information.

Acknowledgements

Instrumentation and technical assistance for this work were provided by the Service Center NMR at Saarland University, with financial support from Saarland University and German Research Foundation DFG (project number 4772985087) and the Service Center X-ray Diffraction, with financial support from Saarland University and German Research Foundation (project number INST 256/506-1). We acknowledge computational resources and support provided by the Imperial College Research Computing Service (http://doi.org/10.14469/hpc/2232). In particular, we thank Jörg Sassmannshausen for installing and testing Psi4.

Supplementary materials

Supplementary material associated with this article can be found, in the online version, at doi:10.1016/j.jil.2023.100060.

References

Alba-Simionesco, C., Tarjus, G., 2022. A perspective on the fragility of glass-forming liquids. J. Non-Crystalline Solids X 14, 100100. doi:10.1016/j.nocx.2022.100100.
Amith, W.D., Araque, J.C., Margulis, C.J., 2022. Ether tails make a large difference for the structural dynamics of imidazolium-based ionic liquids. J. Ion. Liq. 2, 100012. doi:10.1016/j.jil.2021.100012.
Angell, C.Austen, Ansari, Y., Zhao, Z., 2012. Ionic Liquids: past, present and future. Faraday Discuss. 154, 9–27. doi:10.1039/C1FD00112D.
Araque, J.C., Hettige, J.J., Margulis, C.J., 2015. Modern room temperature ionic liquids, a simple guide to understanding their structure and how it may relate to dynamics. J. Phys. Chem. B 119, 12727–12740. doi:10.1021/acs.jpcb.5b05506.
Bauer, V.J., Fulmor, W., Morton, G.O., Safir, S.R., 1968. Restricted rotation in guanidines. J. Am. Chem. Soc. 90, 6846–6847. doi:10.1021/ja01026a052.
Beckmann, J.B.B., Rauber, D., Philippi, F., Goloviznina, K., Ward-Williams, J.A., Sederman, A.J., Mantle, M.D., Pádua, A., Kay, C.W.M., Welton, T., Gladden, L.F., 2022. Molecular dynamics of ionic liquids from fast-field cycling NMR and molecular dynamics simulations. J. Phys. Chem. B doi:10.1021/acs.jpcb.2c01372.
Biernacka, K., Makhlooghiazad, F., Popov, I., Zhu, H., Chotard, J.N., O'Dell, L.A., Sokolov, A.P., Pringle, J.M., Forsyth, M., 2022. Exploration of phase diagram, structural and dynamic behavior of [HMG][FSI] mixtures with NaFSI across an extended composition range. Phys. Chem. Chem. Phys. 24, 16712–16723. doi:10.1039/D2CP01910H.
Borodin, O., Gorecki, W., Smith, G.D., Armand, M., 2010. Molecular dynamics simulation and pulsed-field gradient nmr studies of bis(fluorosulfonyl)imide (FSI) and Bis[(trifluoromethyl)sulfonyl]imide (TFSI)-based ionic liquids. J. Phys. Chem. B 114, 6786–6798. doi:10.1021/jp911950q.
Butschies, M., Sauer, S., Kessler, E., Siehl, H., Claasen, B., Fischer, P., Frey, W., Laschat, S., 2010. Influence of N -alkyl substituents and counterions on the structural and mesomorphic properties of guanidinium salts: experiment and quantum chemical calculations. ChemPhysChem 11, 3752–3765. doi:10.1002/cphc.201000444.
Canongia Lopes, J.N., Shimizu, K., Pádua, A.A.H., Umebayashi, Y., Fukuda, S., Fujii, K., Ishiguro, S., 2008. A tale of two ions: the conformational landscapes of bis(trifluoromethanesulfonyl)amide and N, N -dialkylpyrrolidinium. J. Phys. Chem. B 112, 1465–1472. doi:10.1021/jp076997a.
Cao, Y., Mu, T., 2014. Comprehensive investigation on the thermal stability of 66 ionic liquids by thermogravimetric analysis. Ind. Eng. Chem. Res. 53, 8651–8664. doi:10.1021/ie5009597.
Carrera, G.V.S.M., Frade, R.F.M., Aires-de-Sousa, J., Afonso, C.A.M., Branco, L.C., 2010. Synthesis and properties of new functionalized guanidinium based ionic liquids as non-toxic versatile organic materials. Tetrahedron 66, 8785–8794. doi:10.1016/j.tet.2010.08.040.
Cashen, R.K., Donoghue, M.M., Schmeiser, A.J., Gebbie, M.A., 2022. Bridging database and experimental analysis to reveal super-hydrodynamic conductivity scaling regimes in ionic liquids. J. Phys. Chem. B 126, 6039–6051. doi:10.1021/acs.jpcb.2c01635.
Dhungana, K.B., Faria, L.F.O., Wu, B., Liang, M., Ribeiro, M.C.C., Margulis, C.J., Castner, E.W., 2016. Structure of cyano-anion ionic liquids: x-ray scattering and simulations. J. Chem. Phys. 145, 024503. doi:10.1063/1.4955186.
Dietrich, R.F., Kenyon, G.L., Douglas, J.E., Kollman, P.A., 1980. Barriers to rotation in acylguanidines and acylguanidinium ions. J. Chem. Soc. Perkin Trans. 2, 1592. doi:10.1039/p29800001592.
Dworkin, A., Naumann, R., Seigfred, C., Karty, J.M., Mo, Y., 2005. Y-aromaticity: why is the trimethylenemethane dication more stable than the butadienyl dication? J. Org. Chem. 70, 7605–7616. doi:10.1021/jo0508090.
Fang, S., Tang, Y., Tai, X., Yang, L., Tachibana, K., Kamijima, K., 2011. One ether-functionalized guanidinium ionic liquid as new electrolyte for lithium battery. J. Power Sources 196, 1433–1441. doi:10.1016/j.jpowsour.2010.08.012.
Fang, S., Yang, L., Wang, J., Li, M., Tachibana, K., Kamijima, K., 2009. Ionic liquids based on functionalized guanidinium cations and TFSI anion as potential electrolytes. Electrochim. Acta 54, 4269–4273. doi:10.1016/j.electacta.2009.02.082.
Feng, G., Chen, M., Bi, S., Goodwin, Z.A.H., Postnikov, E.B., Brilliantov, N., Urbakh, M., Kornyshev, A.A., 2019. Free and bound states of ions in ionic liquids, conductivity, and underscreening paradox. Phys. Rev. X 9, 021024. doi:10.1103/PhysRevX.9.021024.
Foreiter, M.B., Gunaratne, H.Q.N., Nockemann, P., Seddon, K.R., Srinivasan, G., 2014. Novel chiral ionic liquids: physicochemical properties and investigation of the internal rotameric behaviour in the neat system. Phys. Chem. Chem. Phys. 16, 1208–1226. doi:10.1039/C3CP53472C.
Frisch, M.J., Trucks, G.W., Schlegel, H.B., Scuseria, G.E., Robb, M.A., Cheeseman, J.R., Scalmani, G., Barone, V., Mennucci, B., Petersson, G.A., Nakatsuji, H., Caricato, M.,

Li, X., Hratchian, H.P., Izmaylov, A.F., Bloino, J., Zheng, G., Sonnenberg, J.L., Hada, M., Ehara, M., Toyota, K., Fukuda, R., Hasegawa, J., Ishida, M., Nakajima, T., Honda, Y., Kitao, O., Nakai, H., Vreven, T., Montgomery, J.A., Peralta, J.E., Ogliaro, F., Bearpark, M., Heyd, J.J., Brothers, E., Kudin, K.N., Staroverov, V.N., Keith, T., Kobayashi, R., Normand, J., Raghavachari, K., Rendell, A., Burant, J.C., Iyengar, S.S., Tomasi, J., Cossi, M., Rega, N., Millam, J.M., Klene, M., Knox, J.E., Cross, J.B., Bakken, V., Adamo, C., Jaramillo, J., Gomperts, R., Stratmann, R.E., Yazyev, O., Austin, A.J., Cammi, R., Pomelli, C., Ochterski, J.W., Martin, R.L., Morokuma, K., Zakrzewski, V.G., Voth, G.A., Salvador, P., Dannenberg, J.J., Dapprich, S., Daniels, A.D., Farkas, O., Foresman, J.B., Ortiz, J.V., Cioslowski, J., Fox, D.J., 2013. Gaussian 09, Revision E.01. Gaussian, Inc., Wallingford CT.

Gasparro, F.P., Kolodny, N.H., 1977. NMR determination of the rotational barrier in N,N-dimethylacetamide. A physical chemistry experiment. J. Chem. Educ. 54, 258. doi:10.1021/ed054p258.

Gobbi, A., Frenking, G., 1993. Y-conjugated compounds: the equilibrium geometries and electronic structures of guanidine, guanidinium cation, urea, and 1,1-diaminoethylene. J. Am. Chem. Soc. 115, 2362–2372. doi:10.1021/ja00059a035.

Gómez, E., Calvar, N., Domínguez, Á., Pesek, K., 2015. Thermal behaviour of pure ionic liquids. In: Ion. Liq. - Curr. State Art. InTech, pp. 199–208. doi:10.5772/59271.

Green, S.M., Ries, M.E., Moffat, J., Budtova, T., 2017. NMR and rheological study of anion size influence on the properties of two imidazolium-based ionic liquids. Sci. Rep. 7, 8968. doi:10.1038/s41598-017-09509-2.

Guerra, J., Bajwa, B., Kumar, P., Vazquez, S., Krishnan, V.V., Maitra, S., 2020. Validation of enthalpy–entropy compensation mechanism in partial amide bond rotation. ACS Omega 5, 9348–9355. doi:10.1021/acsomega.0c00332.

Gutowsky, H.S., Cheng, H.N., 1975. Determination of kinetic parameters by the frequency dependence of the NMR coalescence temperature. J. Chem. Phys. 63, 2439–2441. doi:10.1063/1.431673.

Harris, K.R., 2010. Relations between the fractional Stokes–Einstein and Nernst–Einstein equations and velocity correlation coefficients in ionic liquids and molten salts. J. Phys. Chem. B. 114, 9572–9577. doi:10.1021/jp102687r.

Harris, K.R., 2016. Scaling the transport properties of molecular and ionic liquids. J. Mol. Liq. 222, 520–534. doi:10.1016/j.molliq.2016.07.029.

Harris, K.R., 2019. On the use of the Angell–Walden equation To determine the "ionicity" of molten salts and ionic liquids. J. Phys. Chem. B 123, 7014–7023. doi:10.1021/acs.jpcb.9b04443.

Harris, K.R., Kanakubo, M., 2015. Self-diffusion, velocity cross-correlation, distinct diffusion and resistance coefficients of the ionic liquid [BMIM][Tf 2N] at high pressure. Phys. Chem. Chem. Phys. 17, 23977–23993. doi:10.1039/C5CP04277A.

Harris, K.R., Kanakubo, M., 2016. Self-diffusion coefficients and related transport properties for a number of fragile ionic liquids. J. Chem. Eng. Data. 61, 2399–2411. doi:10.1021/acs.jced.6b00021.

Harris, K.R., Kanakubo, M., Woolf, L.A., 2007. Temperature and pressure dependence of the viscosity of the ionic liquids 1-hexyl-3-methylimidazolium hexafluorophosphate and 1-butyl-3-methylimidazolium bis(trifluoromethylsulfonyl)imide. J. Chem. Eng. Data. 52, 1080–1085. doi:10.1021/je700032n.

Hayes, R., Warr, G.G., Atkin, R., 2015. Structure and nanostructure in ionic liquids. Chem. Rev. 115, 6357–6426. doi:10.1021/cr500411q.

Hofmann, A., Rauber, D., Wang, T.M., Hempelmann, R., Kay, C.W.M., Hanemann, T., 2022. Novel phosphonium-based ionic liquid electrolytes for battery applications. Molecules 27. doi:10.3390/molecules27154729.

Hollóczki, O., Malberg, F., Welton, T., Kirchner, B., 2014. On the origin of ionicity in ionic liquids. Ion pairing versus charge transfer. Phys. Chem. Chem. Phys. 16, 16880–16890. doi:10.1039/C4CP01177E.

Huang, G., Yu, Q., Cai, M., Zhou, F., Liu, W., 2017. Investigation of the lubricity and antiwear behavior of guanidinium ionic liquids at high temperature. Tribol. Int. 114, 65–76. doi:10.1016/j.triboint.2017.04.010.

Hübschle, C.B., Sheldrick, G.M., Dittrich, B., 2011. ShelXle : a Qt graphical user interface for SHELXL. J. Appl. Crystallogr. 44, 1281–1284. doi:10.1107/S0021889811043202.

Hunter, C.A., Packer, M.J., Zonta, C., 2005. From structure to chemical shift and vice-versa. Prog. Nucl. Magn. Reson. Spectrosc. 47, 27–39. doi:10.1016/j.pnmrs.2005.06.001.

Johansson, P., Gejji, S.P., Tegenfeldt, J., Lindgren, J., 1998. The imide ion: potential energy surface and geometries. Electrochim. Acta. 43, 1375–1379. doi:10.1016/S0013-4686(97)10047-0.

Karplus, M., 1963. Vicinal proton coupling in nuclear magnetic resonance. J. Am. Chem. Soc. 85, 2870–2871. doi:10.1021/ja00901a059.

Kashyap, H.K., Annapureddy, H.V.R., Raineri, F.O., Margulis, C.J., 2011. How is charge transport different in ionic liquids and electrolyte solutions? J. Phys. Chem. B 115, 13212–13221. doi:10.1021/jp204182c.

Kashyap, H.K., Hettige, J.J., Annapureddy, H.V.R., Margulis, C.J., 2012. SAXS anti-peaks reveal the length-scales of dual positive–negative and polar–apolar ordering in room-temperature ionic liquids. Chem. Commun. 48, 5103. doi:10.1039/c2cc30609c.

Kashyap, H.K., Santos, C.S., Daly, R.P., Hettige, J.J., Murthy, N.S., Shirota, H., Castner, E.W., Margulis, C.J., 2013. How Does the ionic liquid organizational landscape change when nonpolar cationic alkyl groups are replaced by polar isoelectronic diethers? J. Phys. Chem. B 117, 1130–1135. doi:10.1021/jp311032p.

Köddermann, T., Ludwig, R., Paschek, D., 2008. On the validity of Stokes-Einstein and Stokes-Einstein-Debye relations in ionic liquids and ionic-liquid mixtures. ChemPhysChem 9, 1851–1858. doi:10.1002/cphc.200800102.

Królikowski, M., Więckowski, M., Ebrahiminejadhasanabadi, M., Nelson, W.M., Naidoo, P., Ramjugernath, D., Domańska, U., 2022. Carbon dioxide solubility in ionic liquids: [Guad-(6,6, 1,1, 1,1)][DCA] and [Guad-(6,6, 1,1, 1,1)][TCM] at high pressure. Fluid Phase Equilib. 563, 113572. doi:10.1016/j.fluid.2022.113572.

Lall-Ramnarine, S.I., Zhao, M., Rodriguez, C., Fernandez, R., Zmich, N., Fernandez, E.D., Dhiman, S.B., Castner, E.W., Wishart, J.F., 2017. Connecting structural and transport properties of ionic liquids with cationic oligoether chains. J. Electrochem. Soc. 164, H5247–H5262. doi:10.1149/2.0371708jes.

Lundin, F., Hansen, H.W., Adrjanowicz, K., Frick, B., Rauber, D., Hempelmann, R., Shebanova, O., Niss, K., Matic, A., 2021. Pressure and temperature dependence of local structure and dynamics in an ionic liquid. J. Phys. Chem. B. 125, 2719–2728. doi:10.1021/acs.jpcb.1c00147.

Mahmood, H., Moniruzzaman, M., Yusup, S., Welton, T., 2017. Ionic liquids assisted processing of renewable resources for the fabrication of biodegradable composite materials. Green Chem. 19, 2051–2075. doi:10.1039/C7GC00318H.

Mariani, A., Bonomo, M., Gao, X., Centrella, B., Nucara, A., Buscaino, R., Barge, A., Barbero, N., Gontrani, L., Passerini, S., 2021. The unseen evidence of Reduced Ionicity: the elephant in (the) room temperature ionic liquids. J. Mol. Liq. 324, 115069. doi:10.1016/j.molliq.2020.115069.

McEldrew, M., Goodwin, Z.A.H., Zhao, H., Bazant, M.Z., Kornyshev, A.A., 2021. Correlated ion transport and the gel phase in room temperature ionic liquids. J. Phys. Chem. B. 125, 2677–2689. doi:10.1021/acs.jpcb.0c09050.

Modarresi-Alam, A.R., Najafi, P., Rostamizadeh, M., Keykha, H., Bijanzadeh, H., Kleinpeter, E., 2007. Dynamic 1 H NMR study of the barrier to rotation about the C–N bond in primary carbamates and its solvent dependence. J. Org. Chem. 72, 2208–2211. doi:10.1021/jo061301f.

Moscardini, A., Mezzetta, A., Calisi, N., Caporali, S., Pomelli, C.S., Guazzelli, L., Chiappe, C., 2019. Investigation of a family of structurally-related guanidinium ionic liquids through XPS and thermal analysis. J. Mol. Liq. 277, 280–289. doi:10.1016/j.molliq.2018.12.083.

Nazet, A., Sokolov, S., Sonnleitner, T., Makino, T., Kanakubo, M., Buchner, R., 2015. Densities, viscosities, and conductivities of the imidazolium ionic liquids [Emim][Ac, Emim][FAP, Bmim][BETI, Bmim][FSI, Hmim][TFSI], and [Omim][TFSI]. J. Chem. Eng. Data. 60, 2400–2411. doi:10.1021/acs.jced.5b00285.

Nokami, T., Yamashita, T., Komura, T., Handa, N., Shimizu, M., Yamaguchi, K., Domi, Y., Usui, H., Sakaguchi, H., Itoh, T., 2018. Effects of the ether oxygen atom in alkyl side chains on the physical properties of piperidinium ionic liquids. Faraday Discuss. 206, 523–534. doi:10.1039/C7FD00142H.

Nordness, O., Brennecke, J.F., 2020. Ion dissociation in ionic liquids and ionic liquid solutions. Chem. Rev. 120, 12873–12902. doi:10.1021/acs.chemrev.0c00373.

Palumbo, O., Trequattrini, F., Vitucci, F.M., Paolone, A., 2015. Relaxation dynamics and phase transitions in ionic liquids: viscoelastic properties from the liquid to the solid state. J. Phys. Chem. B 119, 12905–12911. doi:10.1021/acs.jpcb.5b06039.

Philippi, F., Goloviznina, K., Gong, Z., Gehrke, S., Kirchner, B., Pádua, A.A.H., Hunt, P.A., 2022c. Charge transfer and polarisability in ionic liquids: a case study. Phys. Chem. Chem. Phys. 24, 3144–3162. doi:10.1039/D1CP04592J.

Philippi, F., Pugh, D., Rauber, D., Welton, T., Hunt, P.A., 2020b. Conformational design concepts for anions in ionic liquids. Chem. Sci. 11, 6405–6422. doi:10.1039/D0SC01379J.

Philippi, F., Rauber, D., Eliasen, K.L., Bouscharain, N., Niss, K., Kay, C.W.M., Welton, T., 2022b. Pressing matter: why are ionic liquids so viscous? Chem. Sci. 13, 2735–2743. doi:10.1039/d1sc06857a.

Philippi, F., Rauber, D., Kuttich, B., Kraus, T., Kay, C.W.M., Hempelmann, R., Hunt, P.A., Welton, T., 2020a. Ether functionalisation, ion conformation and the optimisation of macroscopic properties in ionic liquids. Phys. Chem. Chem. Phys. 22, 23038–23056. doi:10.1039/D0CP03751F.

Philippi, F., Rauber, D., Palumbo, O., Goloviznina, K., McDaniel, J., Pugh, D., Suarez, S., Fraenza, C.C., Padua, A., Kay, C.W.M., Welton, T., 2022a. Flexibility is the key to tuning the transport properties of fluorinated imide-based ionic liquids. Chem. Sci. 13, 9176–9190. doi:10.1039/D2SC03074H.

Philippi, F., Rauber, D., Zapp, J., Hempelmann, R., 2017. Transport properties and ionicity of phosphonium ionic liquids. Phys. Chem. Chem. Phys. 19, 23015–23023. doi:10.1039/C7CP04552B.

Philippi, F., Rauber, D., Zapp, J., Präsang, C., Scheschkewitz, D., Hempelmann, R., 2018. Multiple ether-functionalized phosphonium ionic liquids as highly fluid electrolytes. ChemPhysChem 20, 443–455. doi:10.1002/cphc.201800939.

Philippi, F., Welton, T., 2021. Targeted modifications in ionic liquids – from understanding to design. Phys. Chem. Chem. Phys. 23, 6993–7021. doi:10.1039/D1CP00216C.

Pratap Singh, A., Sithambaram, D., Sanghavi, R., Kumar Gupta, P., Shanker Verma, R., Doble, M., Gardas, R.L., Senapati, S., 2017. Environmentally benign tetramethylguanidinium cation based ionic liquids. New J. Chem. 41, 12268–12277. doi:10.1039/C7NJ03167J.

Quintana, A.A., Sztapka, A.M., de C. Santos Ebinuma, V., Agatemor, C., 2022. Enabling sustainable chemistry with ionic liquids and deep eutectic solvents: a fad or the future? Angew. Chemie Int. Ed. 61. doi:10.1002/anie.202205609.

Rauber, D., Hofmann, A., Philippi, F., Kay, C.W.M., Zinkevich, T., Hanemann, T., Hempelmann, R., 2021b. Structure-property relation of trimethyl ammonium ionic liquids for battery applications. Appl. Sci. 11, 5679. doi:10.3390/app11125679.

Rauber, D., Philippi, F., Becker, J., Zapp, J., Morgenstern, B., Kuttich, B., Kraus, T., Hempelmann, R., Hunt, P.A., Welton, T., Kay, C.W.M., 2023. Anion and ether group influence in protic guanidinium ionic liquids. Phys. Chem. Chem. Phys. doi:10.1039/D2CP05724G.

Rauber, D., Philippi, F., Kuttich, B., Becker, J., Kraus, T., Hunt, P., Welton, T., Hempelmann, R., Kay, C.W.M., 2021a. Curled cation structures accelerate the dynamics of ionic liquids. Phys. Chem. Chem. Phys. 23, 21042–21064. doi:10.1039/d1cp02889h.

Rauber, D., Philippi, F., Zapp, J., Kickelbick, G., Natter, H., Hempelmann, R., 2018. Transport properties of protic and aprotic guanidinium ionic liquids. RSC Adv. 8, 41639–41650. doi:10.1039/C8RA07412G.

Russina, O., Triolo, A., Gontrani, L., Caminiti, R., Xiao, D., Hines Jr, L.G., Bartsch, R.A., Quitevis, E.L., Plechkova, N., Seddon, K.R., 2009. Morphology and intermolecular dynamics of 1-alkyl-3-methylimidazolium bis{(trifluoromethane)sulfonyl}amide ionic

liquids: structural and dynamic evidence of nanoscale segregation. J. Phys. Condens. Matter. 21, 424121. doi:10.1088/0953-8984/21/42/424121.
Schmidt, J.R., Skinner, J.L., 2003. Hydrodynamic boundary conditions, the Stokes–Einstein law, and long-time tails in the Brownian limit. J. Chem. Phys. 119, 8062–8068. doi:10.1063/1.1610442.
Schreiner, C., Zugmann, S., Hartl, R., Gores, H.J., 2010. Fractional Walden rule for ionic liquids: examples from recent measurements and a critique of the so-called ideal KCl line for the Walden plot †. J. Chem. Eng. Data. 55, 1784–1788. doi:10.1021/je900878j.
Sheldrick, G.M., 2008. A short history of SHELX. Acta Crystallogr. Sect. A Found. Crystallogr. 64, 112–122. doi:10.1107/S0108767307043930.
Sheldrick, G.M., 2015. Crystal structure refinement with SHELXL. Acta Crystallogr. Sect. C Struct. Chem 71, 3–8. doi:10.1107/S2053229614024218.
Shimizu, K., Bernardes, C.E.S., Triolo, A., Canongia Lopes, J.N., 2013. Nano-segregation in ionic liquids: scorpions and vanishing chains. Phys. Chem. Chem. Phys. 15, 16256. doi:10.1039/c3cp52357h.
Singh, S.K., Savoy, A.W., 2020. Ionic liquids synthesis and applications: an overview. J. Mol. Liq. 297, 112038. doi:10.1016/j.molliq.2019.112038.
Suarez, S.N., Rúa, A., Cuffari, D., Pilar, K., Hatcher, J.L., Ramati, S., Wishart, J.F., 2015. Do TFSA anions slither? Pressure exposes the role of TFSA conformational exchange in self-diffusion. J. Phys. Chem. B 119, 14756–14765. doi:10.1021/acs.jpcb.5b08658.
Tang, S., Baker, G.A., Zhao, H., 2012. Ether- and alcohol-functionalized task-specific ionic liquids: attractive properties and applications. Chem. Soc. Rev. 41, 4030. doi:10.1039/c2cs15362a.
Tokuda, H., Hayamizu, K., Ishii, K., Susan, M.A.B.H., Watanabe, M., 2004. Physicochemical properties and structures of room temperature ionic liquids. 1. Variation of anionic species. J. Phys. Chem. B 108, 16593–16600. doi:10.1021/jp047480r.
Tokuda, H., Hayamizu, K., Ishii, K., Susan, M.A.B.H., Watanabe, M., 2005. Physicochemical properties and structures of room temperature ionic liquids. 2. Variation of alkyl chain length in imidazolium cation. J. Phys. Chem. B 109, 6103–6110. doi:10.1021/jp044626d.
Tsunashima, K., Sugiya, M., 2007. Physical and electrochemical properties of low-viscosity phosphonium ionic liquids as potential electrolytes. Electrochem. Commun. 9, 2353–2358. doi:10.1016/j.elecom.2007.07.003.
Ueno, K., Tokuda, H., Watanabe, M., 2010. Ionicity in ionic liquids: correlation with ionic structure and physicochemical properties. Phys. Chem. Chem. Phys. 12, 1649–1658. doi:10.1039/b921462n.
Wang, Y.L., Li, B., Sarman, S., Mocci, F., Lu, Z.Y., Yuan, J., Laaksonen, A., Fayer, M.D., 2020. Microstructural and dynamical heterogeneities in ionic liquids. Chem. Rev. 120, 5798–5877. doi:10.1021/acs.chemrev.9b00693.
Watanabe, M., Thomas, M.L., Zhang, S., Ueno, K., Yasuda, T., Dokko, K., 2017. Application of ionic liquids to energy storage and conversion materials and devices. Chem. Rev. 117, 7190–7239. doi:10.1021/acs.chemrev.6b00504.
Xue, Z., Qin, L., Jiang, J., Mu, T., Gao, G., 2018. Thermal, electrochemical and radiolytic stabilities of ionic liquids. Phys. Chem. Chem. Phys. 20, 8382–8402. doi:10.1039/C7CP07483B.
Yoshii, K., Uto, T., Tachikawa, N., Katayama, Y., 2020. The effects of the position of the ether oxygen atom in pyrrolidinium-based room temperature ionic liquids on their physicochemical properties. Phys. Chem. Chem. Phys. 22, 19480–19491. doi:10.1039/D0CP02662J.
Yu, G., Zhao, D., Wen, L., Yang, S., Chen, X., 2012. Viscosity of ionic liquids: database, observation, and quantitative structure-property relationship analysis. AIChE J. 58, 2885–2899. doi:10.1002/aic.12786.
Yu, J., Zhang, S., Dai, Y., Lu, X., Lei, Q., Fang, W., 2016. Antimicrobial activity and cytotoxicity of piperazinium- and guanidinium-based ionic liquids. J. Hazard. Mater. 307, 73–81. doi:10.1016/j.jhazmat.2015.12.028.
Yuan, W.L., Yang, X., He, L., Xue, Y., Qin, S., Tao, G.H., 2018. Viscosity, conductivity, and electrochemical property of dicyanamide ionic liquids. Front. Chem. 6, 1–12. doi:10.3389/fchem.2018.00059.
Zhang, S., Zhang, Q., Zhang, Y., Chen, Z., Watanabe, M., Deng, Y., 2016. Beyond solvents and electrolytes: ionic liquids-based advanced functional materials. Prog. Mater. Sci. 77, 80–124. doi:10.1016/j.pmatsci.2015.10.001.